Paleoceanography and Paleoclimatology

RESEARCH ARTICLE
10.1029/2023PA004635

Key Points:

- Southern source water expansion during MIS 2, 4, and 6 is consistent with the hypothesis that reduced watermass mixing contributes to lower atmospheric pCO_2
- But Southern source water expansion also occurred during MIS 5e and there is little change in watermass geometry across MIS 5e/d transition
- The MIS 5e carbon isotope profile is systematically lighter than MIS 1 throughout water column, with the largest anomalies above 2,000 m water depth

Correspondence to:
D. C. Lund,
david.lund@uconn.edu

Citation:
Shub, A. B., Lund, D. C., Oppo, D. W., & Garity, M. L. (2024). Brazil Margin stable isotope profiles for the last glacial cycle: Implications for watermass geometry and oceanic carbon storage. *Paleoceanography and Paleoclimatology*, *39*, e2023PA004635. https://doi.org/10.1029/2023PA004635

Received 1 MAR 2023
Accepted 3 NOV 2023

Author Contributions:
Conceptualization: D. C. Lund
Data curation: A. B. Shub, D. C. Lund, D. W. Oppo, M. L. Garity
Formal analysis: A. B. Shub, D. C. Lund, M. L. Garity
Funding acquisition: D. C. Lund
Investigation: A. B. Shub, M. L. Garity
Methodology: A. B. Shub, D. C. Lund, D. W. Oppo
Project Administration: D. C. Lund
Resources: D. W. Oppo
Supervision: D. C. Lund
Validation: M. L. Garity
Writing – original draft: A. B. Shub
Writing – review & editing: D. C. Lund, D. W. Oppo, M. L. Garity

Brazil Margin Stable Isotope Profiles for the Last Glacial Cycle: Implications for Watermass Geometry and Oceanic Carbon Storage

A. B. Shub[1], D. C. Lund[1], D. W. Oppo[2], and M. L. Garity[1]

[1]Department of Marine Sciences, University of Connecticut, Groton, CT, USA, [2]Department of Geology and Geophysics, Woods Hole Oceanographic Institution, Woods Hole, MA, USA

Abstract Vertical profiles of benthic foraminiferal oxygen and carbon isotopes ($\delta^{18}O$ and $\delta^{13}C$) imply the volume of southern source water (SSW) in the Atlantic basin expanded during the Last Glacial Maximum. Shoaling of the boundary between SSW and northern source water (NSW) may reduce mixing between the two watermasses, thereby isolating SSW and enhancing its ability to store carbon during glacial intervals. Here we test this hypothesis using profiles of $\delta^{18}O$ and $\delta^{13}C$ from the Brazil Margin spanning the last glacial cycle (0–150 ka). Shoaling of the SSW-NSW boundary occurred during Marine Isotope Stage (MIS) 2, 4, and 6, consistent with expansion of SSW and greater carbon sequestration in the abyss. But the watermass boundary also shoaled during MIS 5e, when atmospheric CO_2 levels were comparable to MIS 1. Additionally, we find there was little change in watermass structure across the MIS 5e-d transition, the first major decline in CO_2 of the last glacial cycle. Thus, the overall pattern in glacial-interglacial geometry is inconsistent with watermass mixing acting as a primary control on atmospheric pCO_2. We also find that $\delta^{13}C$ values for MIS 5e are systematically lower than MIS 1, with the largest difference (~1‰) occurring in the upper water column. Low $\delta^{13}C$ during MIS 5e was most likely due to a long-term imbalance in weathering and deposition of calcium carbonate or input of ^{13}C-depleted carbon from a reservoir external to the ocean-atmosphere system.

1. Introduction

Glacial terminations over the last 800,000 years were marked by abrupt increases in atmospheric CO_2 of 80–100 ppm (Lüthi et al., 2008; Neftel et al., 1982; Petit et al., 1999). While orbital forcing initiates glacial-interglacial transitions (Huybers & Wunsch, 2005; Imbrie et al., 1992), atmospheric CO_2 is often invoked as an important amplifier of deglaciation (Broecker, 1982; Genthon et al., 1987; Shakun et al., 2012). Because the ocean contains ~50 times more carbon than the atmosphere, glacial-interglacial CO_2 oscillations are most likely regulated by oceanic processes (Sigman & Boyle, 2000). A range of mechanisms have been proposed, including changes in biological export production (Jaccard et al., 2016; Martínez-García et al., 2014), Southern Ocean Sea ice extent (Morales Maqueda & Rahmstorf, 2002; Stephens & Keeling, 2000), air-sea disequilibrium (Khatiwala et al., 2019), and deep ocean circulation (Ferrari et al., 2014; Toggweiler, 1999). Glacial-interglacial CO_2 variability is likely due to a combination of these factors.

In contrast to abrupt increases in atmospheric CO_2 during terminations, glacial inception is characterized by a stepwise decrease in CO_2. During the last glacial cycle (0–150 ka), the primary intervals of drawdown occurred at the Marine Isotope Stages (MIS) 5e/d and MIS 5a/4 transitions. In each case, atmospheric CO_2 declined 30–40 ppm and remained low for tens of thousands of years (Eggleston et al., 2016). The CO_2 decline at the MIS 5e/d boundary may have been due to sea ice expansion in the Southern Ocean, while the decline at the MIS 5a/4 transition was apparently due to reduced ventilation of the abyssal ocean (Kohfeld & Chase, 2017). Persistently low atmospheric CO_2 levels into MIS 2 may have been caused by expansion of Antarctic Bottom Water (AABW), isolation of its associated deep overturning cell, and enhanced sequestration of carbon in the abyss (Ferrari et al., 2014). During glacial terminations, retreat of sea ice in the Southern Ocean and contraction of AABW should promote CO_2 release. Here we evaluate deep South Atlantic watermass geometry during MIS 1–6 using vertical profiles of benthic foraminiferal $\delta^{18}O$ and $\delta^{13}C$ from the Brazil Margin.

Benthic foraminiferal $\delta^{18}O$ and $\delta^{13}C$ provide complimentary information on watermass distributions in the geologic past. The $\delta^{18}O$ of calcite is a conservative tracer because it varies as a function of the temperature and the $\delta^{18}O$ of seawater, which is linearly related to salinity. After the equilibrium $\delta^{18}O$ of calcite is set at the sea

10.1029/2023PA004635

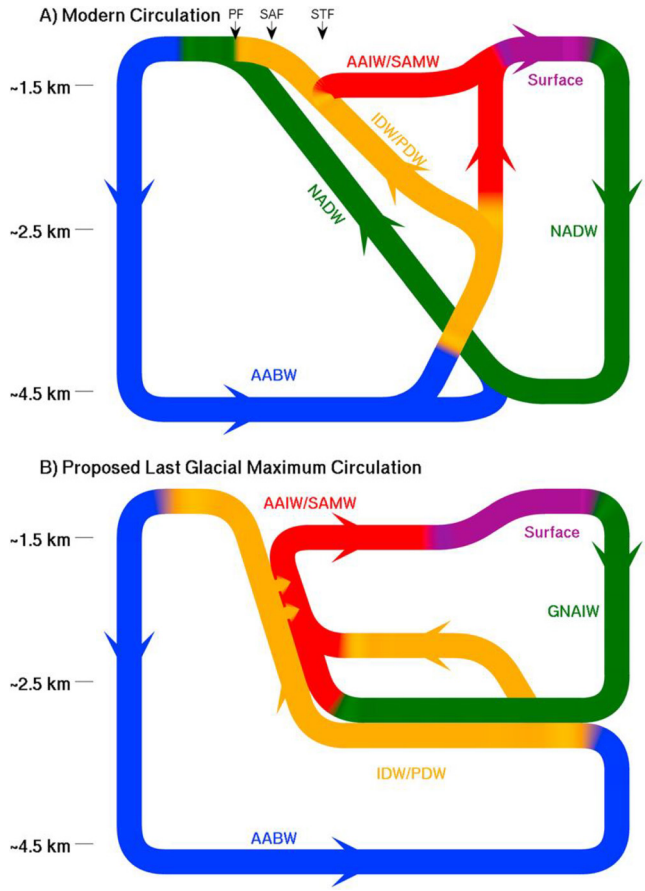

Figure 1. Schematic meridional overturning circulation for (a) the modern and (b) Last Glacial Maximum (LGM) (after Sikes et al. (2017)). In the modern ocean, rough bottom topography promotes diapycnal mixing between AABW and NADW, creating a "Figure 8" circulation belt that promotes ventilation of the abyss. During the LGM, shoaling of the boundary between northern and southern source water results in reduced ventilation of the abyssal Atlantic. Watermasses are abbreviated as follows: Pacific Deep Water (PDW), Indian Deep Water (IDW), Antarctic Bottom Water (AABW), North Atlantic Deep Water (NADW), Glacial North Atlantic Intermediate Water (GNAIW), Antarctic Intermediate Water (AAIW), and Sub-Antarctic Mode Water (SAMW).

surface, it will only change through advection and mixing in the ocean interior. Benthic $\delta^{18}O$ is therefore a conservative tracer that can be used to map deep ocean watermasses in the geologic past (Lund et al., 2011). The $\delta^{13}C$ of benthic foraminifera, which records the $\delta^{13}C$ of dissolved inorganic carbon (DIC), is non-conservative because it is influenced by the ocean circulation and remineralization of organic matter. Benthic foraminiferal $\delta^{13}C$ therefore reflects distinct watermasses and the influence of isotopically light respired carbon. Used in tandem, $\delta^{18}O$ and $\delta^{13}C$ can be used to map watermass boundaries and highlight regions where remineralization influences the $\delta^{13}C$ tracer field (Gebbie, 2014; J. L. Hoffman & Lund, 2012). $\delta^{13}C$ can also be used to infer watermasses in cases where spatial gradients in $\delta^{18}O$ are small.

In the modern Atlantic Ocean, the overturning circulation consists of two distinct but related cells; a deep southern component branch that includes AABW and an upper northern component branch that includes NADW (Figure 1). Today, the upper boundary of AABW is defined by the neutral density $\gamma = 28.15$ kg/m^3 (Lumpkin & Speer, 2007). (Unlike density surfaces that are tied to discrete reference pressures, neutral surfaces better reflect density across a range of water depths (Jackett & McDougall, 1997).) The $\gamma = 28.15$ kg/m^3 surface is located at approximately 3,500 m water depth in the South Atlantic (Lund et al., 2011), where breaking of internal waves over rough topography facilitates diapycnal mixing between the upper and lower cells (Polzin et al., 1997; St. Laurent et al., 2002; Wunsch & Ferrari, 2004). Mixing of AABW with NADW creates a quasi-continuous "Figure 8" circulation belt that enhances ventilation of AABW, facilitating release of CO_2 to the atmosphere (Ferrari et al., 2014; Marshall & Speer, 2012) (Figure 1a). For the remainder of the paper, we refer to bottom water originating from the Southern Ocean as Southern Source Water (SSW), rather than AABW. We also use Northern Source Water (NSW) to refer to deep waters originating from the North Atlantic, rather than NADW or Glacial North Atlantic Intermediate Water.

During glacial times, separation of the northern and southern cells may have increased carbon sequestration in the abyssal ocean. Movement of the watermass boundary away from the zone of intense mixing near the seafloor should facilitate separation of the overturning cells, limit ventilation of SSW, and promote sequestration of carbon in the abyss (Adkins, 2013; Ferrari et al., 2014; Toggweiler, 1999). Benthic $\delta^{18}O$ of foraminifera from the Brazil Margin and Blake Ridge indicate the boundary between NSW and SSW was located between 2,500 and 3,000 m during the Last Glacial Maximum (LGM) (Curry & Oppo, 2005; J. L. Hoffman & Lund, 2012; Keigwin, 2004). By comparison, the boundary was located between 3,000 and 3,500 m during the late Holocene (J. L. Hoffman & Lund, 2012; Lund et al., 2011). Thus, the Holocene and the LGM represent contrasting circulation states in the abyssal Atlantic, with the former representing a restricted version of SSW and the latter an expanded version that is relatively isolated. If expansion and contraction of SSW plays a primary role in regulating atmospheric CO_2 during the last glacial cycle, we should observe an LGM-like expanded version of SSW during MIS 6 and a Holocene-like contracted version during MIS 5e. We should also observe watermass boundary shoaling across the MIS 5e/d and MIS 5a/4 transitions.

The last interglacial period (MIS 5e) had CO_2 levels similar to the late Holocene (Indermühle et al., 1999; Petit et al., 1999) but it was different in a number of other important respects. First, boreal summertime insolation early in MIS 5e was greater than MIS 1 (Otto-Bliesner et al., 2013; Yin & Berger, 2011), northern hemisphere mean annual surface temperatures were 1–2°C warmer than preindustrial values (Otto-Bliesner et al., 2013; Turney & Jones, 2010) and global mean sea level was 4–5 m higher (Clark et al., 2020; Dyer et al., 2021). Relatively little is known about the state of the ocean circulation during MIS 5e, though benthic foraminiferal $\delta^{13}C$ results suggest the geometry of Atlantic watermasses was similar to today (Kohfeld & Chase, 2017). An extended period of

Table 1
Summary of Location, Age Model, and Stable Isotope Results for KNR-159-5 Cores

Core	Water depth (m)	Latitude	Longitude	Age model	Stable isotopes
36GGC	1,268	−27.52	−46.47	Sortor and Lund (2011) and This paper	Curry and Oppo (2005)
39JPC	1,265	−27.26	−46.48	This paper	This paper
78GGC	1,822	−27.49	−46.34	Tessin and Lund (2013) and This paper	Tessin and Lund (2013)
79JPC	1,830	−27.49	−46.33	This paper	Garity et al. (2024)
42JPC	2,293	−27.76	−46.03	J. L. Hoffman and Lund (2012) and This paper	Curry and Oppo (2005) and Garity et al. (2024)
30GGC	2,503	−29.13	−46.06	Tessin and Lund (2013) and This paper	Tessin and Lund (2013)
31JPC	2,514	−29.13	−46.06	This paper	This paper
63GGC	2,732	−28.36	−45.84	Lund et al. (2015) and This paper	Lund et al. (2015)
64JPC	2,732	−28.36	−45.84	This paper	This paper
20JPC	2,951	−28.64	−45.54	Lund et al. (2015) and This paper	Lund et al. (2015) and This paper
126JPC	3,584	−29.53	−45.08	This paper	This paper
125GGC	3,589	−29.53	−45.08	J. L. Hoffman and Lund (2012) and This paper	J. L. Hoffman and Lund (2012)

weakened AMOC during Termination II and early MIS 5e may have contributed to higher sea-level via subsurface oceanic warming and erosion of ice shelves (Clark et al., 2020; Deaney et al., 2017).

In this paper, we use benthic foraminiferal $\delta^{18}O$ and $\delta^{13}C$ to reconstruct South Atlantic watermass geometry for the last glacial cycle. We estimate the depth of the NSW-SSW boundary for MIS 1–6 using vertical profiles of $\delta^{18}O$ and $\delta^{13}C$ from the Brazil Margin and discuss the implications for watermass mixing and atmospheric CO_2. We also show that $\delta^{13}C$ at the Brazil Margin was systematically lower during MIS 5e and discuss the implications for carbon exchange between oceanic and external carbon reservoirs.

2. Methods

2.1. Core Location and Sampling

The sediment cores used for this study were collected from 27° to 30°S in the western South Atlantic (Table 1). The hydrography in this region is influenced by northern and southern watermasses, including Upper Circumpolar Deep Water (UCDW), NADW, and AABW (Figure 2). Our analysis focused on nine cores spanning the depth range from 1,300 m to 3,900 m. Seven of the nine jumbo piston cores provided adequate carbonate preservation and oxygen isotope stratigraphy to merit detailed study, including KNR159-5-39JPC, 79JPC, 42JPC, 31JPC, 64JPC, 20JPC, and 126JPC (for the remainder of the paper we exclude the KNR159-5 prefix for simplicity). Several other piston cores from the Brazil Margin were sampled but excluded from this study due to either a lack of *C. wuellerstorfi* or inadequate length to penetrate MIS 6 (121JPC at 3,300 m, 46JPC at 3,400 m, and 23JPC at 3,900 m). Previous studies generated stable isotope results using companion gravity cores to focus on the LGM and deglaciation (Table 1); we use these results here to create time series that encompass MIS 1–6.

Core samples were taken at approximately 8 cm resolution from each core, spanning the time intervals from MIS 3 (~30 ka) through MIS 6 (~145 ka). Sediment samples were freeze-dried for 48 hr, washed through a 63-μm sieve, and then dried at 40°C. Each sample was picked for benthic foraminifera (*Cibicidoides wuellerstorfi*) from the >250-μm size fraction. Core 39JPC contained very few *C. wuellerstorfi sensu stricto* (Gottschalk et al., 2016). The vast majority of specimens in core 39JPC were instead similar to *C. wuellerstorfi sensu lato*, characterized by chambers that are slightly inflated relative to *C. wuellerstorfi* and with fewer total chambers in the final whorl (Gottschalk et al., 2016).

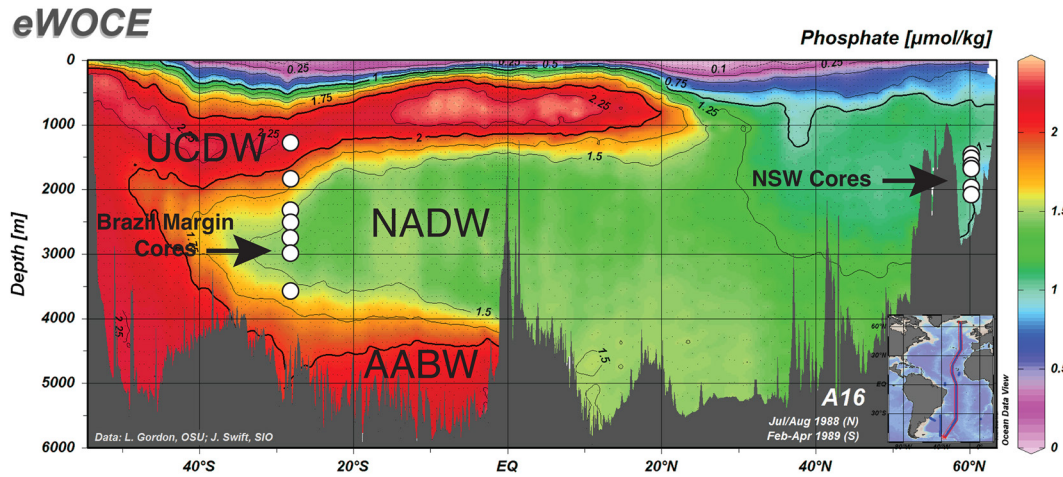

Figure 2. Core locations for this study superimposed on the World Ocean Circulation Experiment (WOCE) A16 phosphate section (Schlitzer, 2000). The hydrography at the Brazil Margin core sites (1,800–3,600 m) is influenced by Upper Circumpolar Deep Water (UCDW), North Atlantic Deep Water (NADW), and Antarctic Bottom Water (AABW). Cores from 1,400 to 2,000 m water depth in the North Atlantic (~60°N) are used to estimate the endmember composition of Northern Source Water (NSW), including EW9302-8JPC (Oppo et al., 1997, 2001), ODP 162–983 (Channell et al., 1997; Raymo et al., 2004), ODP 162–984 (Came et al., 2007; Praetorius et al., 2008; Raymo et al., 2004), EW9302-16JPC, EW9302-15JPC, and EW9302-14JPC (Oppo et al., 1997).

Foraminifera were analyzed for $\delta^{18}O$ and $\delta^{13}C$ using standard procedures (Ostermann & Curry, 2000). Stable isotope analyses were performed on individual tests to facilitate identification of bioturbated intervals. In rare cases, two tests were used when the individual foraminifera were too small to yield an adequate amount of CO_2 for stable isotope analysis. Samples for this study were run on a triple-collector gas source mass spectrometer coupled to a Kiel IV automated preparation device at the Stable Isotope Laboratory at the University of Michigan. Data were converted to Vienna Pee Dee Belemnite (VPDB) using NBS 19 (n = 48, $\delta^{13}C = 1.96 \pm 0.04$, $\delta^{18}O = -2.18 \pm 0.08$‰) and NBS 18 ($n$ = 13, $\delta^{13}C = -5.01 \pm 0.05$, $\delta^{18}O = -22.97 \pm 0.09$‰). We also used the Atlantis II standard (n = 26, $\delta^{13}C = 0.91 \pm 0.06$, $\delta^{18}O = 3.45 \pm 0.06$‰) to monitor mass spectrometer performance at the heavy end of the $\delta^{18}O$ spectrum, where many of the benthic results fall (>3.5‰). Data for KNR159-5-39JPC were generated at the Woods Hole Oceanographic Institution (WHOI) using a Finnigan MAT 253 coupled to Kiel IV automated device. The WHOI data were converted to VPDB using NBS 19 (n = 82, $\delta^{13}C = 1.95 \pm 0.05$, $\delta^{18}O = -2.19 \pm 0.10$‰). Results for Atlantis II standards run at WHOI (n = 90, $\delta^{13}C = 0.85 \pm 0.08$, $\delta^{18}O = 3.51 \pm 0.09$‰) were similar to those run at the University of Michigan.

Table 2
Planktonic Radiocarbon Results

Core	Depth (cm)	^{14}C age (years)	1σ error (years)	Calendar age (yr B.P.)	1σ error (years)
79JPC	240.5	33,780	400	37,913	447
79JPC	272.5	41,400	1,000	43,741	1,020
79JPC	320.5	41,230[a]	1,000	N/A	N/A
42JPC	112.5	21,750	80	25,247	215
42JPC	136.5	26,020	160	29,508	256
42JPC	176.5	33,330	380	37,375	429

Note. All samples were run at UC Irvine and ^{14}C results are based on *G. ruber* and *T. sacculifer*, with a typical combined weight of 3 mg. Calendar ages and uncertainties determined using Bchron (see methods for details).
[a]Age reversal.

2.2. Age Models

Age models for the Brazil Margin cores are based on a combination of radiocarbon and oxygen isotope stratigraphy. Published ^{14}C dates were used to constrain the age models for cores 78GGC (Tessin & Lund, 2013), 42JPC (Curry & Oppo, 2005; J. L. Hoffman & Lund, 2012), 30GGC (Tessin & Lund, 2013), 63GGC (Lund et al., 2015), 20JPC (Lund et al., 2015), and 125GGC (J. L. Hoffman & Lund, 2012). Additional ^{14}C dates were generated for cores 79JPC and 42JPC (Table 2). Each sample was picked for planktonic foraminifera (*G. ruber* and *T. sacculifer*) from the >250 µm size fraction, with total sample weights for ^{14}C analyses ranging from 1 to 5 mg. Samples were prepared for radiocarbon dating at the Keck Carbon Cycle Accelerated Mass Spectrometer Laboratory at the University of California Irvine as outlined in Tessin and Lund (2013). Calendar ages were calibrated using the MARINE20 calibration curve (Heaton et al., 2020; Reimer et al., 2020) and the software package Bchron (Haslett & Parnell, 2008; https://andrewcparnell.github.io/Bchron/). The modern ΔR near the Brazil Margin is -130 ± 49, calculated using the 10 closest estimates of surface water reservoir age to the core sites

Table 3
Age Intervals Used to Define Marine Isotope Stages[a]

MIS	1	2	4	5a	5b	5c	5d	5e	6a	6b
Age (kyr)	0–5	19–23	61–69	69–87	87–96	96–105	104–117	120–128	133–143	143–150+

[a]Intervals based on MIS naming convention of Railsback et al. (2015), ages based on the deep South Atlantic stack of Lisiecki and Stern (2016). We define MIS 5e as 120–128 ka to avoid low $\delta^{18}O$ values associated with meltwater input during T2 (Oppo et al., 2001).

(Reimer & Reimer, 2001; http://calib.org/marine/). To account for regional changes in the reservoir age in the geologic past, we assumed a ΔR error of ± 200 years (1σ).

Prior to 45 ka, age models for the Brazil Margin cores are based on oxygen isotope stratigraphy. We aligned the benthic $\delta^{18}O$ records with the Lisiecki and Stern (2016) (LS16) $\delta^{18}O$ stack of deep South Atlantic cores (2,000–5,000 m; 70°S-0; 70°W-30°E). We use LS16 because of its regionally specific nature and improvements in age control during TII and MIS 5e (Lisiecki & Stern, 2016). The Brazil Margin $\delta^{18}O$ records were first visually aligned with the LS16 stack using the relative amplitude of $\delta^{18}O$ signals within each record. Age model tie points were then determined by aligning intervals with the maximum rate of change (i.e., during transitions between marine isotope stages). Ages for depths between tie points were determined by linear interpolation. The main sources for uncertainty in the resulting age models include sampling resolution in each core (0.5–2 kyr), age uncertainty in the LS16 stack (2–4 kyr from 38 to 112 ka, 5 kyr from 113 to 127 ka, and 4 kyr from 128 to 145 ka), and depth-dependent $\delta^{18}O$ lags that occur in the Atlantic during glacial terminations (1–2 kyr) (Lund et al., 2015; Waelbroeck et al., 2011).

2.3. Vertical Profiles and Watermass Boundaries

Using the benthic foraminiferal time series, we generated vertical profiles of $\delta^{18}O$ and $\delta^{13}C$ for MIS 1, 2, 4, 5, and 6. Separate profiles were also created for each sub-stage of MIS 5 (a, b, c, d, and e). We chose not to develop profiles for MIS 3 given limited age control during this long (~30 kyr) interval. The time windows used to define each stage are summarized in Table 3. When selecting data to calculate mean values, points on or near the transition to neighboring isotope stages were excluded to ensure accurate estimates of $\delta^{18}O$ and $\delta^{13}C$. In a few isolated cases, bioturbated individual foraminifera could be clearly identified by anomalous $\delta^{18}O$ and $\delta^{13}C$ values. These values were excluded from the profiles. We also excluded the lone data point from the MIS 5d interval in core 31JPC. In this case the $\delta^{18}O$ value appeared to be valid in the context of the 31JPC time series because it was higher than values from MIS 5c and 5e. But it was >0.8‰ greater than any other $\delta^{18}O$ value in the MIS 5d profile, which is physically implausible. The stable isotope values for this foraminifer ($\delta^{18}O = 4.3$‰, $\delta^{13}C = 0.7$‰) imply it was most likely bioturbated from the youngest portion of MIS 6.

The vertical profiles were used to determine the boundary between northern and southern component waters during each marine isotope stage. Following the procedure outlined in Lund et al. (2011), we calculated the uncertainty for each mean $\delta^{18}O$ value by combining the sampling uncertainty (i.e., the $\delta^{18}O$ standard error) with a calibration uncertainty of 0.18‰. The calibration uncertainty accounts for scatter in the relationship between core top foraminiferal $\delta^{18}O$ and predicted $\delta^{18}O$ based on in situ temperature and seawater $\delta^{18}O$ (Marchal & Curry, 2008). This is likely a conservative error given that the calibration is based on regressing $\delta^{18}O$ results from non-modern core tops onto water column properties, which have both spatial and temporal variability. In the few cases where only one $\delta^{18}O$ analysis was available, we used a sampling uncertainty of 0.4‰, which is based on the highest standard errors of multi-analysis means in the data set. We then generated 1,000 profiles where each $\delta^{18}O$ value was randomly sampled from a Gaussian distribution based on the combined sampling and calibration uncertainty. Each profile was sampled at 200 m depth increments to eliminate bias associated the unequal spacing of the Brazil Margin cores (J. L. Hoffman & Lund, 2012). The resulting profiles were used to estimate the vertical $\delta^{18}O$ gradient ($\delta^{18}O_z$) over a 400 m water depth range, varying the center point from 1,500 to 3,300 m in 200 m increments. We interpret the depth where $\delta^{18}O_z$ is greatest to represent the boundary between NSW and SSW. For the $\delta^{13}C$ profiles, we used the same approach but instead applied a calibration uncertainty of 0.14‰, which is based on the scatter in core top foraminiferal $\delta^{13}C$ versus the $\delta^{13}C$ of DIC in bottom waters (Duplessy et al., 1984; Lund et al., 2011).

Table 4
Locations of North Atlantic Records Used in This Paper

Core	Water depth (m)	Latitude	Longitude	Age model	Stable isotopes
EW9302-16JPC	1,451	61.94	−23.88	This paper	Oppo et al. (1997)
EW9302-15JPC	1,522	62.72	−23.98	This paper	Oppo et al. (1997)
ODP 162-984	1,649	61.43	−24.08	This paper	Raymo et al. (2004), Came et al. (2007), and Praetorius et al. (2008)
EW9302-14JPC	1,653	61.42	−24.11	This paper	Oppo et al. (1997)
EW9302-8JPC	2,102	60.81	−25.05	This paper	Oppo et al. (1997) and Oppo et al. (2001)
ODP 162-983	1,984	60.40	−23.64	This paper	Channell et al. (1997) and Raymo et al. (2004)

2.4. Northern Source Water

Stable isotope records from an additional six sediment core records were compiled from the literature to constrain the endmember composition of NSW (Table 4). The endmember stable isotope values for NSW are based on records from >50°N and from 1,000 to 2,000 m water depth. Locations further south or deeper in the water column can be influenced by SSW. The age model for each core was determined by visual alignment with the intermediate (1,000–2,000 m) North Atlantic $\delta^{18}O$ stack of Lisiecki and Stern (2016). This was particularly important for determining $\delta^{18}O$ and $\delta^{13}C$ values during MIS 5e because the foraminiferal $\delta^{18}O$ minimum in this region is offset from the MIS 5e time interval (120–128 ka) due to input of meltwater during TII (Lisiecki & Stern, 2016; Oppo et al., 2001). In all cases, we used NSW timeseries based on *C. wuellerstorfi*, which reliably records the $\delta^{13}C$ of DIC (Duplessy et al., 1984; Schmittner et al., 2017). Interlaboratory offsets of up to 0.3‰ for $\delta^{18}O$ (Hodell et al., 2003; Ostermann & Curry, 2000) makes comparison of $\delta^{18}O$ data from different labs more challenging, especially when spatial $\delta^{18}O$ gradients are small (<0.5‰).

3. Results

3.1. Age Models

The age models show a monotonic increase in age with depth, as expected under conditions of continuous sediment deposition. Accumulation rates vary markedly within each core, however (Figure 3). During glacial stages sedimentation rates generally exceed 10 cm/kyr while during interglacial stages rates are generally less than 5 cm/kyr. The glacial-interglacial contrast in sedimentation rate occurs in both the ^{14}C- and $\delta^{18}O$-constrained portions of the records, implying that the $\delta^{18}O$-based ages (i.e., those older than 45 ka) provide a reliable estimate of the age-depth relationship.

For this study, a total of six new radiocarbon dates were generated for cores 42JPC and 79JPC. In 42JPC, the ages increase monotonically with depth, extending the existing ^{14}C age control to approximately 37 kyr BP (Table 2; Figure 3). The ages for 79JPC have larger uncertainties because the samples are older and have little ^{14}C remaining (fraction modern ∼0.006) (Table 2). The date at 320.5 cm in 79JPC is out of stratigraphic order and we therefore exclude it from the age model. Given the age of this sample (∼40 ka), it has no impact on the stable isotope time series during MIS 1–2 and MIS 4–6, which are the focus of this study.

3.2. Stable Isotope Time Series

The Brazil Margin benthic $\delta^{18}O$ records follow the anticipated sawtooth pattern due to glacial-interglacial variations in ice volume and temperature. Each record has distinct interglacial stages (MIS 1 and 5) and glacial stages (MIS 2, 4, and 6) (Figure 4). The substages of MIS 5 are also apparent, including 5a, 5d, 5c, 5d, and 5e. The deeper Brazil Margin $\delta^{18}O$ timeseries plot more or less on top of the Lisiecki and Stern (2016) deep Atlantic stack (gray line in Figure 4), while the shallower records are 0.4–0.8‰ lighter. In isolated cases, bioturbated foraminifera can be identified by their anomalous $\delta^{18}O$ and $\delta^{13}C$ values (open symbols in Figure 4). These values were not included in the running averages or vertical profiles.

The $\delta^{13}C$ records generally show the expected pattern of more negative values during glacial intervals, particularly in the deeper cores, where the glacial-interglacial signal amplitude is >0.5‰ (Figure 4). In contrast, the

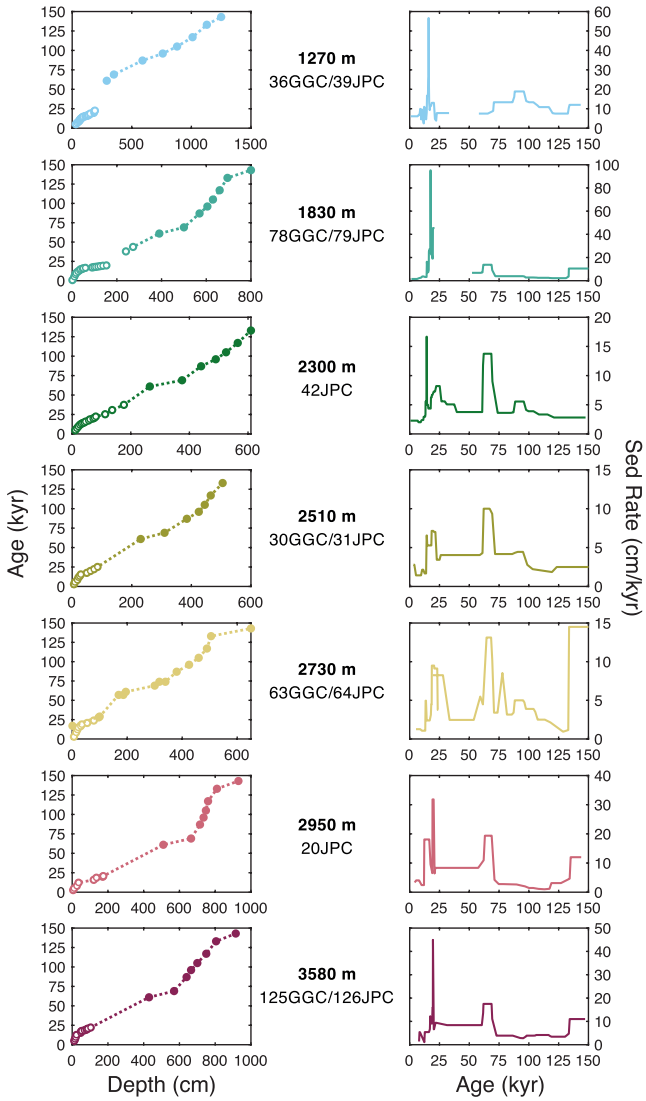

Figure 3. Age models (left column) and implied down-core sedimentation rates (right column) for the cores in this study. The results are displayed in order of water depth, from the shallowest core in the top row (~1,300 m) to deepest in the bottom row (~3,600 m). Calendar-calibrated ^{14}C ages are indicated by open symbols, while age control points based on oxygen isotope stratigraphy are shown as closed symbols. A 3-point running average was applied to radiocarbon-based ages to mitigate unrealistic changes in sediment accumulation due to the combined effect of age uncertainty and closely spaced data points.

shallowest core has only modest glacial-interglacial variability and it is characterized by a long-term positive trend in $\delta^{13}C$. A subtle long-term trend is also apparent at 1,800 m. At 1,800 m and 2,300 m, there are millennial-scale negative $\delta^{13}C$ anomalies during glacial-interglacial transitions, including MIS 6-5e, MIS 5d-c, MIS 5b-a, MIS 4-3, and MIS 2-1. The origin of the signals is discussed in Garity et al. (2024). In general, the mean $\delta^{13}C$ for each Brazil Margin core decreases with increasing water depth. More positive values reflect the influence of NSW and more negative values reflect SSW. The exception is core 39JPC at ~1,300 m where $\delta^{13}C$ is lighter than at mid-depths (1,500–2,500 m), due to the influence of ^{13}C-depleted shallow SSW, analogous to UCDW in the modern South Atlantic.

3.3. Vertical Profiles and Watermass Characteristics

3.3.1. MIS 1

The primary influence on the vertical profile of $\delta^{18}O$ is temperature. In the modern Southwest Atlantic, potential temperature decreases by ~5°C from 500 to 1,000 m (whp-atlas.ucsd.edu/atlantic_index.html), equivalent to an increase in the equilibrium $\delta^{18}O$ of calcite of ~1.2‰ (Marchitto et al., 2014). The anticipated $\delta^{18}O$ signal is consistent with that observed in benthic foraminifera during MIS 1 (Figure 5a). Deeper in the water column, from ~1,000 to 3,000 m, there is relatively little variation in benthic $\delta^{18}O$, which reflects the similar temperature of UCDW and NADW at the Brazil Margin. Below 3,000 m, however, temperatures decrease by ~2°C due to the influence of AABW, which should yield a ~0.5‰ increase in equilibrium $\delta^{18}O$. Consistent with this prediction, benthic $\delta^{18}O$ during MIS 1 increases by 0.5 ± 0.1‰ below 3 km water depth (Figure 5a). The maximum vertical gradient in $\delta^{18}O$ (i.e., $\delta^{18}O_z$) during MIS 1 occurs at approximately 3,200 m (Figure 6a). A second less pronounced maximum occurs near 2,300 m, but this is likely due to the number of cores used in this study (n = 7). The more detailed profile (n = 24 cores) lacks such a feature (J. L. Hoffman & Lund, 2012).

Benthic $\delta^{13}C$ provides a complimentary perspective on the watermasses present at the Brazil Margin. The MIS 1 $\delta^{13}C$ vertical profile based on cores in this study (Figure 5b) is similar to published profiles that have greater vertical resolution (Curry & Oppo, 2005; J. L. Hoffman & Lund, 2012). The $\delta^{13}C$ minimum at 1,300 m is due to the influence of UCDW, the $\delta^{13}C$ maximum at 2,500 m is associated with ^{13}C-enriched NADW, and low $\delta^{13}C$ values below 3,000 m reflect the influence of ^{13}C-depleted AABW (Figure 5b). The maximum vertical gradient in $\delta^{13}C$ ($\delta^{13}C_z$) occurs at approximately 3,200 m water depth (Figure 6b), similar to the depth of maximum $\delta^{18}O_z$. Thus, during MIS 1, both $\delta^{18}O$ and $\delta^{13}C$ indicate the boundary between NADW and AABW was located between 3,000 and 3,500 m. The pattern of high $\delta^{13}C$ NADW sandwiched between low $\delta^{13}C$ UCDW and AABW is a characteristic feature of the Southwest Atlantic today and during the late Holocene (Curry & Oppo, 2005; J. L. Hoffman & Lund, 2012). The three primary watermasses are also apparent in the $\delta^{13}C$ versus $\delta^{18}O$ mixing diagram (Figure 7a). The MIS 1 results for the cores presented in this study reflect the influence UCDW, NADW, and AABW.

3.3.2. MIS 2

Similar to MIS 1, benthic $\delta^{18}O$ values for MIS 2 increase monotonically with depth, increasing from 4.2 ± 0.1‰ at 1,300 m to 4.7 ± 0.1‰ at 3,600 m (Figure 5a). Maximum $\delta^{18}O_z$ values occur from ~2,200 to 2,600 m during MIS 2 (Figure 6c), compared to ~3,000–3,300 m during MIS 1 (Figure 6a). The $\delta^{13}C$ profile for MIS 2 is characterized by low $\delta^{13}C$ near 1,300 m, a distinct maximum at 1,800 m, and low $\delta^{13}C$ below 2,500 m (Figure 5b).

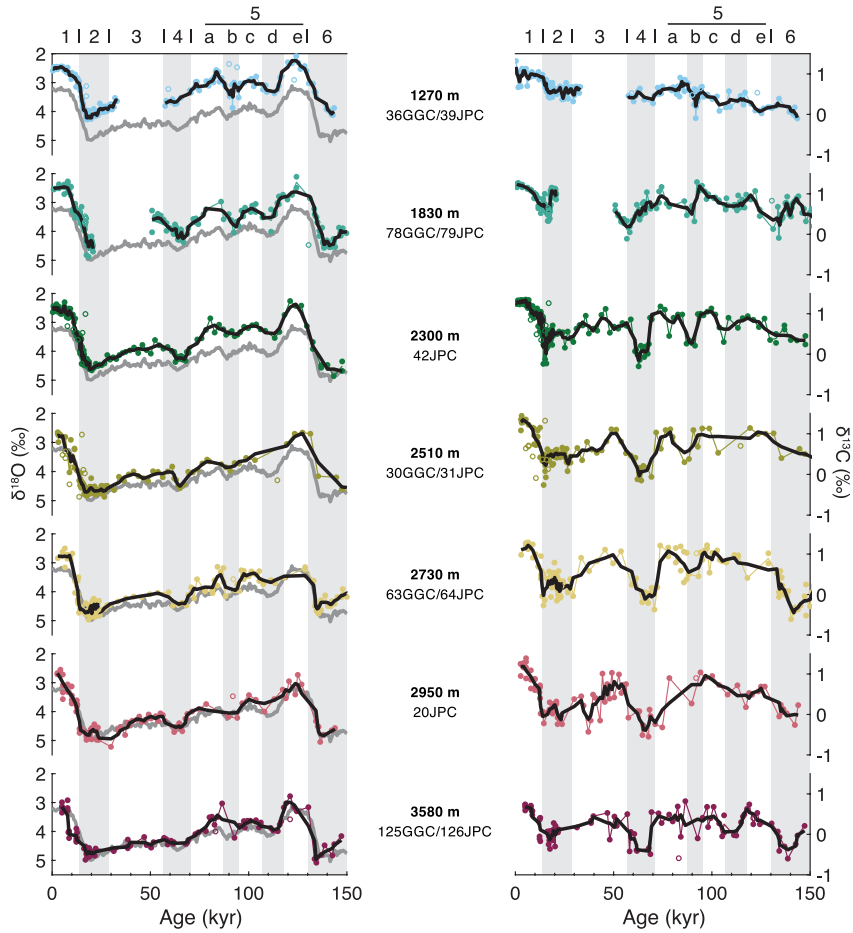

Figure 4. Stable isotope results for the Brazil Margin cores. (Left column) $\delta^{18}O$ time series, and (Right column) $\delta^{13}C$ time series, using the age models in Figure 3. Results for each core are plotted as individual benthic foraminiferal results (circles), the average value at each stratigraphic level (thin colored line), and a simple 3-point running average (black line). Bioturbated shells (open symbols) are not included in the running averages. Each $\delta^{18}O$ record is superimposed on the LS16 deep South Atlantic benthic $\delta^{18}O$ stack (gray line) (Lisiecki & Stern, 2016). Marine Isotope Stages 1–6 are indicated at top with glacial intervals (MIS 2, 4, 5b, 5d, and 6) in gray shading.

Maximum $\delta^{13}C_z$ values occur near 2,000 m during MIS 2 (Figure 6d), compared to ~3,200 m during MIS 1 (Figure 6b). Both the $\delta^{18}O$ and $\delta^{13}C$ profiles indicate the boundary between SSW and NSW was at least 500 m shallower during MIS 2. The data imply that sSSW, NSW, and SSW influenced the Brazil Margin during MIS 2 (Figure 7b). sSSW has higher $\delta^{13}C$ than SSW but lower $\delta^{18}O$. NSW has a higher $\delta^{13}C$ than either southern watermass, but its $\delta^{18}O$ is similar to that of sSSW, making it difficult to discern using $\delta^{18}O$ alone. MIS 2 stable isotope results from 1,800 to 4,000 m fall along a well-defined mixing line; the 1,800 m site is heavily influenced by NSW while the 3,600 m site is heavily influenced by SSW (Figure 7b).

3.3.3. MIS 4

Of all of the results summarized here, the $\delta^{13}C$ data from MIS 4 are the most distinct. Benthic $\delta^{13}C$ data from 2,000 to 3,000 m are more depleted than any other time in the last 150 ka (Figure 5d). The shift between MIS 5a and 4 is particularly striking; $\delta^{13}C$ values below 2,000 km decreased by nearly 1‰, while those at 1,300 m and 1,800 m remained largely unchanged. Not surprisingly, the highest $\delta^{13}C_z$ values during MIS 4 occur between 1,800 and 2,200 m (Figure 6f), similar to the depth range of maximum $\delta^{13}C_z$ results for MIS 2 (Figure 6d). The $\delta^{18}O$ profile for MIS 4 is similar to MIS 2 but with values that are 0.2–0.3‰ lower throughout the water column (Figure 5c). Maximum $\delta^{18}O_z$ values for MIS 4 fall primarily between 1,400 and 1,700 m (Figure 6d). Together, the $\delta^{18}O_z$ and $\delta^{13}C_z$ results imply the NSW-SSW boundary during MIS 4 was at its shallowest point of the last glacial cycle.

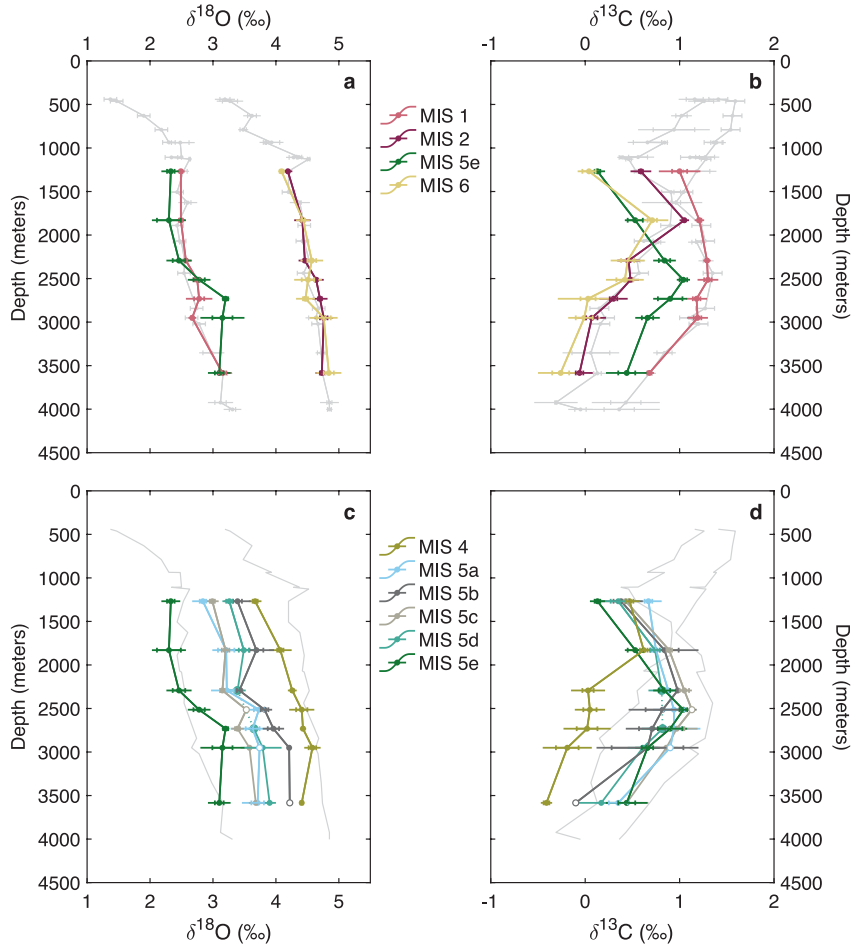

Figure 5. Vertical profiles of Brazil Margin $\delta^{18}O$ (panels a and c) and $\delta^{13}C$ (panels b and d) for the last glacial cycle. Colored profiles represent data from this study. Gray profiles for the Holocene and Last Glacial Maximum are based on data from Curry and Oppo (2005) and J. L. Hoffman and Lund (2012). Each data point represents the mean stable isotope value for a given Marine Isotope Stage. Horizontal bars indicate the $\pm 1\sigma$ uncertainty, while vertical notches are the standard error. Open symbols indicate time intervals constrained by one data point. Note that core 31JPC at 2,500 m water depth lacks data for MIS 5d (see Section 3 for details).

The MIS 4 results from 1,800 to 3,600 m can be explained by two-component mixing between SSW and NSW. The $\delta^{18}O$-$\delta^{13}C$ pair at 1,800 m water depth falls near the NSW endmember while results for the deeper sites cluster near the SSW endmember (which we assume is represented by the deepest results at the Brazil Margin) (Figure 8a). This is in contrast to MIS 2 and 6, when $\delta^{18}O$-$\delta^{13}C$ pairs are more evenly distributed along the NSW-SSW mixing line (Figures 7b and 8c). Thus, the vertical profiles, NSW-SSW watermass boundary, and mixing diagram all highlight greater influence of SSW at the Brazil Margin during MIS 4.

3.3.4. MIS 5a-d

Benthic $\delta^{13}C$ results for MIS 5a-d reveal a watermass structure similar to MIS 1. The $\delta^{13}C$ profiles for each sub-stage are characterized by low values in the shallowest and deepest parts of the water column, with relatively high values in between (Figure 5d). Maximum $\delta^{13}C_z$ values generally fall in the 2,500 m–3,200 m depth range (Figure 6). Given the paucity of *C. wuellerstorfi* in some sections, the profiles are not as well constrained as MIS 1, however. For example, the results at 2,500 m during MIS 5c, 2,950 m during MIS 5a, and 3,600 m during MIS 5b are each based on one stable isotope analysis (Figure 5). And there are no data available at 2,500 m during MIS 5d. Despite these limitations, we were able to generate coherent vertical profiles using results from adjacent cores.

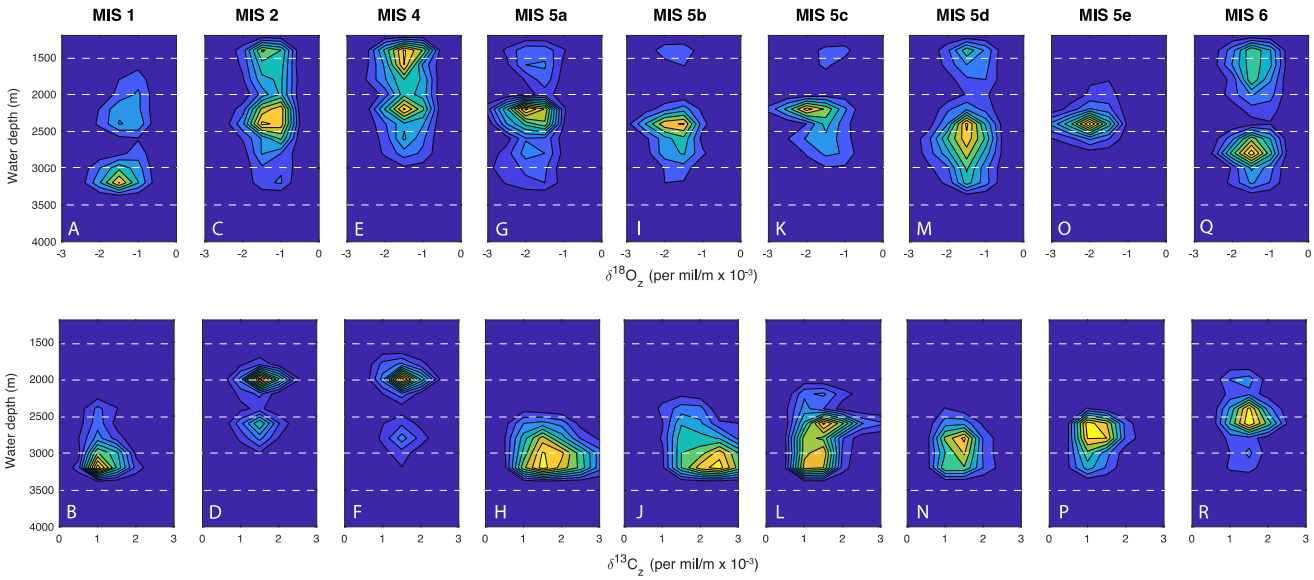

Figure 6. Probability density functions (PDFs) for $\delta^{18}O_z$ (top row) and $\delta^{13}C_z$ (bottom row) versus water depth for MIS 1 through 6. Maximum $\delta^{18}O_z$ and $\delta^{13}C_z$ values during MIS 1 occur from 3,000 m to 3,500 m, the approximate boundary between NSW and SSW (Lund et al., 2011). Maximum $\delta^{18}O_z$ and $\delta^{13}C_z$ values during glacial stages MIS 2, 4, and 6 occur at least 500 m shallower in the water column. The pattern for MIS 5 is more complex; the PDFs for $\delta^{18}O$ overlap those for glacial stages MIS 2, 4, and 6, while the PDFs for $\delta^{13}C$ overlap with that for MIS 1. Maximum $\delta^{18}O_z$ and $\delta^{13}O_z$ for MIS 5e occur shallower in the water column than their respective maxima during MIS 1.

As anticipated, the benthic $\delta^{18}O$ profiles for MIS 5a-d are positively offset from the profile for MIS 1 (Figure 5c). The glacial substages (MIS 5b, d) are also enriched relative to interglacial substages (MIS 5a, c). For each substage, maximum $\delta^{18}O_z$ values occur between ~2,100 and 2,800 m (Figure 6). Overall, the $\delta^{13}C$ and $\delta^{18}O$ results suggest three watermasses were present at the Brazil Margin during MIS 5a-d, including sSSW, NSW, and SSW, similar to the modern configuration of UCDW, NADW and AABW. The mixing diagram for MIS 5d is consistent with mixing of three endmember components (Figure 8b). Mixing diagrams for MIS 5a-c display a similar pattern (not shown).

3.3.5. MIS 5e

The vertical profiles for MIS 5e are remarkably different than during MIS 1. Benthic $\delta^{18}O$ during MIS 5e is more depleted above 2,500 m and more enriched below 2,500 m (Figure 5a). As a result, the maximum in $\delta^{18}O_z$ occurs at ~2,400 m (Figure 6o), about 800 m shallower than MIS 1 (Figure 6a). Maximum $\delta^{18}O_z$ values for MIS 5e are also more tightly clustered in depth than MIS 1. Equally surprising are the $\delta^{13}C$ results for MIS 5e, which are lower than MIS 1 throughout the water column (Figure 5b). Offsets of 0.5–1‰ are observed above 2,000 m water depth, while smaller offsets (~0.3‰) occur below 2,000 m. Maximum $\delta^{13}C_z$ values during MIS 5e are centered at ~2,700 m (Figure 6p), somewhat deeper than the $\delta^{18}O_z$ maximum, but still 500 m shallower than during MIS 1 (Figure 6b). Thus, both the $\delta^{18}O_z$ and $\delta^{13}C_z$ results indicate the boundary between NSW and SSW shoaled substantially during MIS 5e. The overall shape of the MIS 5e $\delta^{13}C$ profile is consistent with MIS 1, however, with ^{13}C-enriched NSW sandwiched between ^{13}C-depleted shallow SSW and SSW. The same three watermasses are apparent in the $\delta^{13}C$ versus $\delta^{18}O$ mixing diagram (Figure 8d).

3.3.6. MIS 6

Unlike MIS 5e and MIS 1, the results for MIS 6 and 2 are very similar to one another. Benthic $\delta^{18}O$ increased from 4.1 ± 0.1‰ at 1,300 m to 4.8 ± 0.1‰ at 3,600 m during MIS 6, indistinguishable from the MIS 2 values (Figure 5a). The highest $\delta^{18}O$ and lowest $\delta^{13}C$ during MIS 2 and 6 occurs at 3,600 m, consistent with SSW influencing the abyssal Southwest Atlantic (Figures 5a and 5b). The MIS 6 $\delta^{13}C$ profile also has a secondary minimum in $\delta^{13}C$ at 1,300 m, highlighting the presence of sSSW. Benthic $\delta^{13}C$ was ~0.5‰ lower at 1,300 m during MIS 6 than MIS 2, however (Figure 5b). It was also ~0.3‰ lower at 1,800 m. Both the MIS 2 and 6 profiles display a $\delta^{13}C$ maximum at 1,800 m, likely NSW (Figure 5b). The mixing diagrams for MIS 2 and 6 are quite similar, highlighting three familiar watermass endmembers, including sSSW, NSW, and SSW (Figures 7b and 8c). The

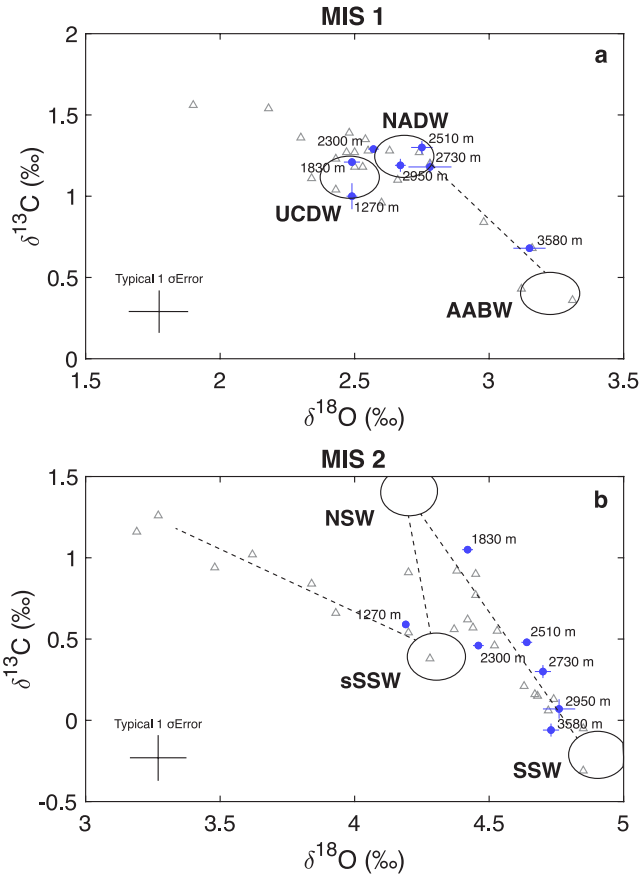

Figure 7. Cross-plots of $\delta^{18}O$ versus $\delta^{13}C$ for Brazil Margin cores, including (a) MIS 1 and (b) MIS 2. Results from this study (blue circles) are projected onto data from J. L. Hoffman and Lund (2012) and Curry and Oppo (2005) (gray triangles). During MIS 2, three watermasses were present in the Southwest Atlantic, including shallow Southern Source Water (sSSW), Northern Source Water (NSW), and Southern Source Water (SSW). $\delta^{18}O$ values (<4‰) are due to mixing with glacial Sub-Antarctic Mode Water (GSAMW) (Tessin & Lund, 2013). MIS 2 results fall primarily on a mixing line between SSW and NSW. Error bars indicate the standard error for the mean $\delta^{18}O$ and $\delta^{13}C$ at each water depth. Note that the $\delta^{18}O$ and $\delta^{13}C$ absolute values in each panel are different but each span a range of 2‰.

main difference between MIS 2 and 6 is the depth of the NSW-SSW boundary. Maximum $\delta^{18}O_z$ values for MIS 6 are centered at ~2,800 m (Figure 6q), about 400 m deeper than during MIS 2. The maximum $\delta^{13}C_z$ for MIS 6 occurs at ~2,500 m (Figure 6q), or ~500 m deeper than during MIS 2. Thus, both the $\delta^{18}O$ and $\delta^{13}C$ profiles indicate the boundary between NSW and SSW was deeper during MIS 6.

4. Discussion

The main objective of this study was to reconstruct the boundary between NSW and SSW during the last glacial cycle using vertical profiles of $\delta^{18}O$ and $\delta^{13}C$. Prior work at the Brazil Margin showed the boundary shoaled approximately 500 m during MIS 2, possibly leading to reduced mixing between SSW and NSW and enhanced carbon sequestration in the abyss. It has been hypothesized that shoaling was due to greater sea ice extent and brine formation in the Southern Ocean, which filled the deep Atlantic with cold and salty SSW (Ferrari et al., 2014). Two related predictions follow from this hypothesis, including: (a) shoaling of the SSW-NSW boundary should occur during other glacial intervals with low atmospheric pCO_2 (MIS 4 and 6) and (b) interglacial intervals (MIS 1 and MIS 5e) with reduced sea ice extent and high pCO_2 should have a watermass structure similar to today.

4.1. Consistent Watermass Geometry During Glacial Maxima

We first address whether shoaling occurred during glacial maxima. As outlined in the results section, vertical profiles for MIS 2 and 6 suggest the two glacial stages were similar, with each characterized by a shallow NSW-SSW boundary (Figure 6). The relatively shallow glacial boundary compared to MIS 1 implies that a larger volume of the deep South Atlantic was occupied by SSW. Reduced NSW influence is also apparent in the $\delta^{18}O$ versus $\delta^{13}C$ mixing diagrams for MIS 2 and 6, with stable isotope results generally falling on the mixing line between NSW and SSW (Figures 7b and 8c). By comparison, MIS 1 data from 1,800 to 3,000 m cluster closely around the NSW endmember (Figure 7a), highlighting its greater influence at these water depths during the Holocene.

Placing the Brazil Margin results in the context of other western Atlantic data shows that the deep Atlantic was influenced by similar watermasses during MIS 2 and 6. In both intervals, the deep Atlantic was filled with ^{13}C-depleted SSW below ~2,500 m and relatively ^{13}C-enriched NSW above (Figures 9b and 9d). We attribute the enhanced vertical gradient in $\delta^{13}C$ to shoaling of the watermass boundary and separation of the upper and lower circulation cells (Adkins, 2013; Lund et al., 2011). While the $\delta^{13}C$ results suggest SSW penetrated into the North Atlantic, the $\delta^{18}O$ sections yield a different picture. High (>4.5‰) $\delta^{18}O$ values are observed in the deep South Atlantic during MIS 2 and 6, consistent with the presence of SSW, but high $\delta^{18}O$ values are not observed in the deep tropical Atlantic during either time interval (Figures 10b and 10d). In both MIS 2 and 6, the $\delta^{18}O$ difference between the South Atlantic and tropical Atlantic (~0.5‰) is comparable to lab intercalibration offsets (up to 0.4‰), so the spatial pattern needs to be verified with further work. Taken at face value, however, the $\delta^{18}O$ sections imply the deep North Atlantic was influenced primarily by NSW rather than SSW, consistent with recent εNd compilations for MIS 2 (Du et al., 2020; Pöppelmeier et al., 2020). Together, the $\delta^{18}O$ and εNd data suggest low $\delta^{13}C$ values in the deep North Atlantic were due to remineralization rather than northward incursion of SSW.

Estimates of glacial watermass geometry in the Atlantic depend on the number and type of data employed. For example, one inversion of $\delta^{13}C$, $\delta^{18}O$, and Cd/Ca results for MIS 2 suggests remineralization may have caused NSW to "masquerade" as SSW (Gebbie, 2014). Another inversion, using improved age constraints but fewer

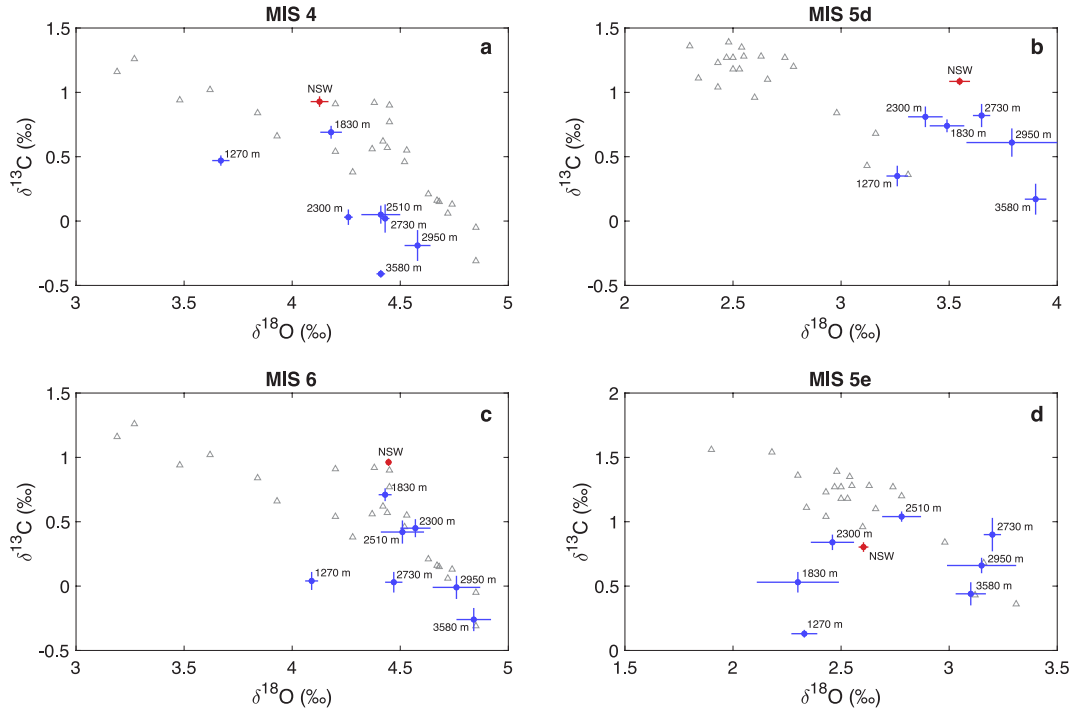

Figure 8. Cross-plots of Brazil Margin $\delta^{18}O$ and $\delta^{13}C$ for (a) MIS 4, (b) MIS 5d, (c) MIS 6, and (d) MIS 5e. Panels (a and c) show results from this study (blue circles) projected onto MIS 2 data from J. L. Hoffman and Lund (2012) and Curry and Oppo (2005) (gray triangles). Panels (b and d) display results from MIS 5d and 5e projected onto MIS 1 data. The NSW endmember (red circle) is calculated from subpolar North Atlantic cores in Figure 11. Error bars indicate the standard error on the mean $\delta^{18}O$ and $\delta^{13}C$ at each water depth.

$\delta^{13}C$ and $\delta^{18}O$ data, suggests ^{13}C-depleted values were instead associated with SSW (Oppo et al., 2018). In each study, all of the tracer data are used simultaneously to find a best fit solution. As a result, the solution tends to favor $\delta^{13}C$ and Cd/Ca, which display similar spatial patterns during MIS 2. A third inverse study examined $\delta^{18}O$ and $\delta^{13}C$ tracer fields independently and found that LGM $\delta^{18}O$ data were consistent with the modern circulation, while $\delta^{13}C$ data were not (Marchal & Curry, 2008). Future inversion studies using intercalibrated $\delta^{18}O$ data from MIS 2, 4, and 6 will be necessary to determine whether the watermass distributions were indeed different than today.

4.2. SSW Expansion During MIS 4

SSW occupied a greater portion of the water column during MIS 4 than either MIS 2 or 6. The expansion is apparent in the vertical profiles for MIS 4, where waters below 2,000 m water depth are characterized by high $\delta^{18}O$ and low $\delta^{13}C$ (Figure 5). The uniqueness of the profiles is further highlighted by vertical gradients in $\delta^{18}O$ and $\delta^{13}C$. Maximum $\delta^{18}O_z$ values occur primarily from 1,500 to 2,000 m, or ~500 m shallower than MIS 2 and 6 (Figure 6). Maximum $\delta^{13}C_z$ values for MIS 4 occur near 2,000 m, which is similar to MIS 2 but ~500 m shallower than MIS 6.

The Brazil Margin $\delta^{13}C$ results are consistent with the broader pattern in the western Atlantic during MIS 4. Our compilation shows that low $\delta^{13}C$ waters are found below 2,000 m in the South Atlantic (Figure 9f). The Kohfeld and Chase (2017) compilation, which combined data from the eastern and western basins, also shows ^{13}C-depleted waters in the North Atlantic during MIS 4. The $\delta^{18}O$ section presents a different picture, however, where high $\delta^{18}O$ SSW is limited to the South Atlantic (Figure 10f). Thus, the $\delta^{18}O$ and $\delta^{13}C$ sections yield conflicting pictures of deep Atlantic watermass geometry during MIS 4, similar to the disagreement observed during glacial maxima. It is therefore possible that remineralization causes NSW to masquerade as SSW not only during MIS 2 (Gebbie, 2014), but also during MIS 4 and 6.

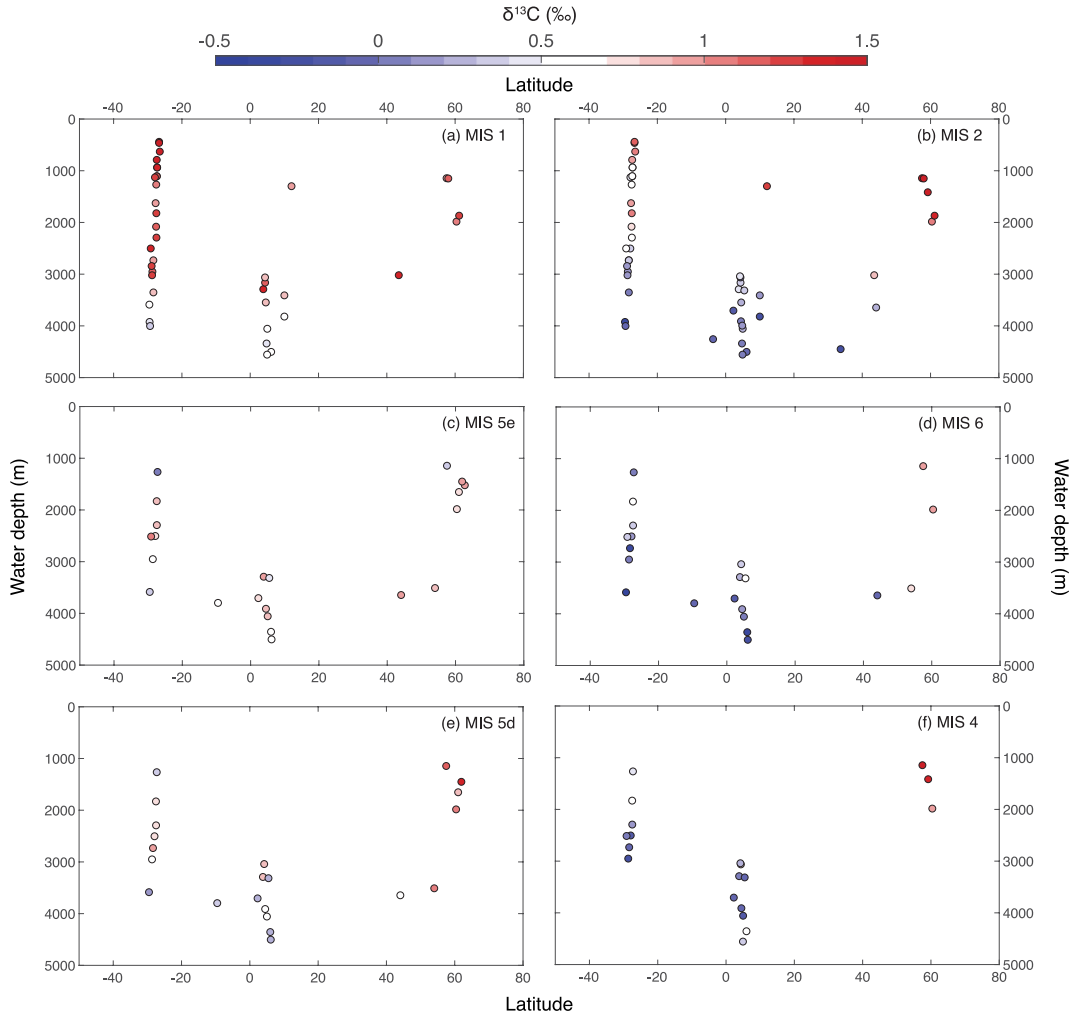

Figure 9. Compilation of $\delta^{13}C$ results from the western Atlantic for (a) MIS 1, (b) MIS 2, (c) MIS 5e, (d) MIS 6, (e) MIS 5d, and (f) MIS 4. Data from Channell et al. (1997), Oppo et al. (1997, 2001), Raymo et al. (2004), Curry and Oppo (2005), Came et al. (2007), Praetorius et al. (2008), Oliver et al. (2010), J. L. Hoffman and Lund (2012), and this study. Age models for all cores were updated using the $\delta^{18}O$ stacks in Lisiecki and Stern (2016) for specific regions of the Atlantic.

4.3. Watermass Boundary Shoaling During MIS 5e

At the beginning of the discussion section, we posited that glacial intervals should be characterized by shoaling of the SSW-NSW boundary, while interglacial intervals should have a watermass structure similar to today. As anticipated, we find that shoaling occurred during MIS 2, 4 and 6, but we also find that the shoaling occurred during MIS 5e. Maximum $\delta^{18}O_z$ values occur from 2,300 to 2,600 m, compared to 3,000–3,400 m for MIS 1 (Figure 6). Thus, our results do not support the idea that all interglacial intervals are characterized by a deep watermass boundary and enhanced mixing between deep overturning cells. According to the geometric argument presented in Ferrari et al. (2014), we would expect the watermass boundary during MIS 5e to be deeper than today, given more limited sea ice extent in the Southern Ocean during the last interglacial period, particularly in the Atlantic sector (Crosta et al., 2022; Holloway et al., 2017). Reduced sea ice cover was likely due to warming in the Southern Ocean (~2°C at 128 ka) (Capron et al., 2014, 2017; J. S. Hoffman et al., 2017), perhaps associated with a weaker AMOC and reduced northward oceanic heat transport early in MIS 5e (Holloway et al., 2018).

We speculate that boundary shoaling was due to a relatively weak AMOC early in MIS 5e and a change in the buoyancy of NSW. Our vertical $\delta^{18}O$ profile implies the relative $\delta^{18}O$ contrast between NSW and SSW was larger during MIS 5e (Figure 5a), perhaps due to input of ^{18}O-depleted meltwater into the North Atlantic. The $\delta^{18}O$ of NSW was 2.5 ± 0.2‰ during MIS 5e (Figure 11), compared to 2.7 ± 0.1‰ for the Holocene (Lund et al., 2015).

10.1029/2023PA004635

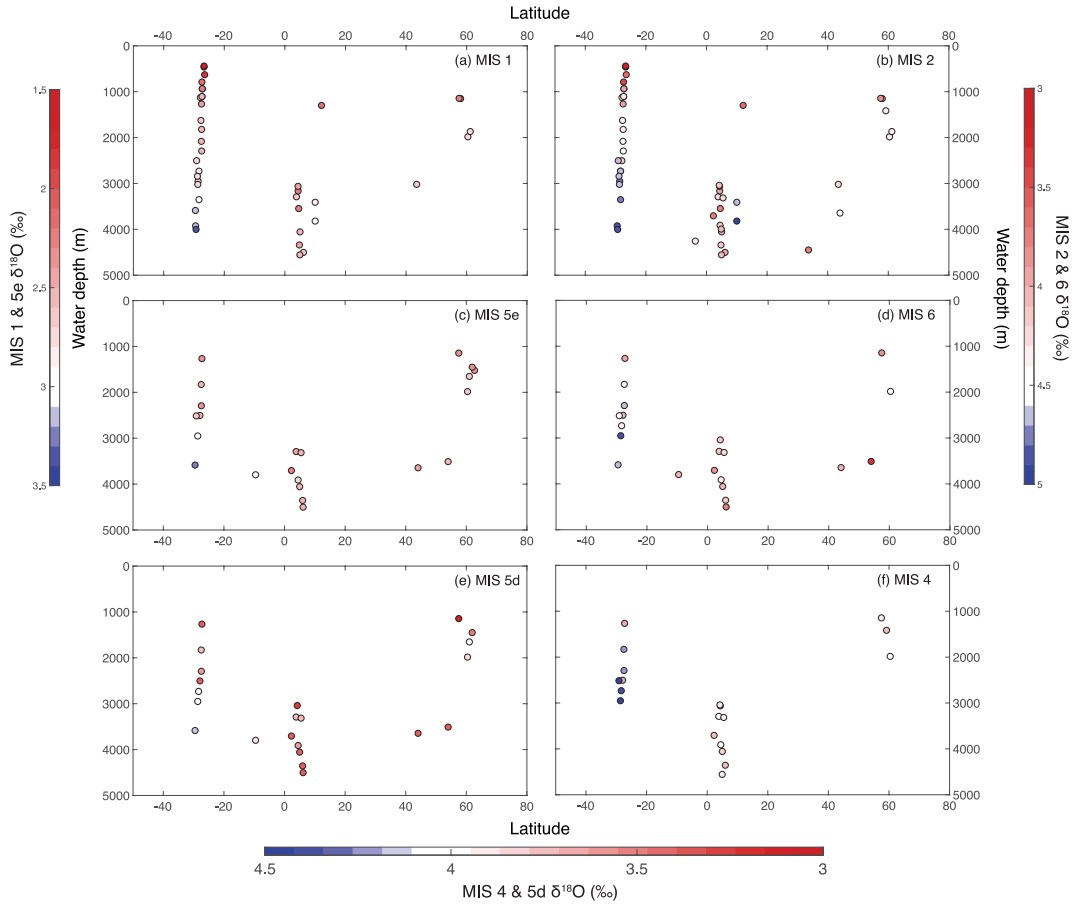

Figure 10. Compilation of $\delta^{18}O$ results from the western Atlantic for (a) MIS 1, (b) MIS 2, (c) MIS 5e, (d) MIS 6, (e) MIS 5d, and (f) MIS 4. To account for the difference in mean $\delta^{18}O$ between time intervals, different $\delta^{18}O$ data ranges were used for glacial stages (MIS 2 and 6), interglacial stages (MIS 1 and 5e), and intermediate stages (MIS 4 and 5d). See Figure 9 caption for data sources.

Given that the contrast (0.2‰) is similar to interlaboratory offsets, additional $\delta^{18}O$ analyses are required to verify the endmember $\delta^{18}O$ estimates.

The overall watermass structure was similar during MIS 1 and 5e, despite differences in the NSW-SSW boundary depth. Three watermasses are apparent in the MIS 5e $\delta^{13}C$ profile, including ^{13}C-enriched NSW and ^{13}C-depleted sSSW and SSW (Figure 5b). The same watermasses are apparent in the $\delta^{13}C$ versus $\delta^{18}O$ mixing diagram (Figure 8d). The position of NSW in the mixing diagram is unusual, however. Instead of plotting as a clear endmember, as it does during other isotope stages, it falls amongst the middepth Brazil Margin results. The overall pattern in the mixing diagram implies NSW had a reduced influence at the Brazil Margin. While other circulation proxies suggest AMOC recovery had occurred by the beginning of MIS 5e (Böhm et al., 2015; Deaney et al., 2017), benthic $\delta^{13}C$ records from the upper North Atlantic show a lagged response (Figure 11), perhaps due to the residual influence of a weakened AMOC. Toward the end of MIS 5e, the $\delta^{13}C$ of NSW overlaps with that of the middepth Brazil Margin sites (~1‰), implying NSW had become fully re-established in the South Atlantic.

4.4. Evolution of South Atlantic Watermass Geometry During Glacial Inception

In the preceding sections, we discussed watermass geometry during glacial maxima and full interglacial conditions. In this section, we focus on Brazil Margin watermass geometry during glacial inception. In particular, we address whether boundary shoaling occurred during the MIS 5e/d and MIS 5a/4 transitions, the two main intervals of atmospheric CO_2 decline of the last glacial cycle.

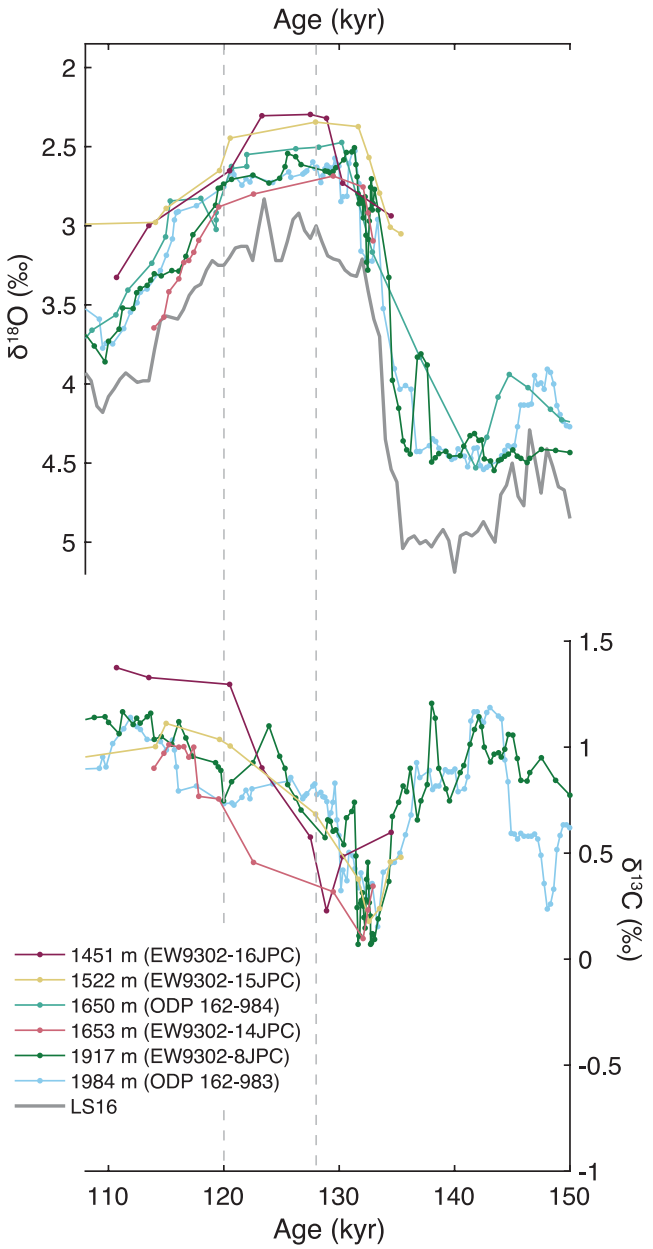

Figure 11. Published records of $\delta^{18}O$ (top) and $\delta^{13}C$ (bottom) from subpolar North Atlantic cores spanning 1,400–2,000 m water depth. Note that $\delta^{13}C$ for ODP 162–984 was based on a mixture of *Cibicidoides* species so it is neither shown above nor included in NSW endmember estimate. North Atlantic cores include EW9302-8JPC (Oppo et al., 1997, 2001), ODP 162–983 (Channell et al., 1997; Raymo et al., 2004), ODP 162–984 (Came et al., 2007; Praetorius et al., 2008; Raymo et al., 2004), EW9302-16JPC, EW9302-15JPC, and EW9302-14JPC (Oppo et al., 1997). The $\delta^{18}O$ results are superimposed on the LS16 intermediate North Atlantic stack (1,000–2,000 m) (gray line) (Lisiecki & Stern, 2016). Core locations are shown in Figure 2.

In the case of MIS 5e/d, there is little change in watermass structure at the Brazil Margin. The vertical $\delta^{13}C$ profiles for MIS 5e and 5d are similar to one another, with each showing $\delta^{13}C$ maxima between 2,000 and 3,000 m (NSW) and $\delta^{13}C$ minima shallower (sSSW) and deeper in the water column (SSW) (Figure 5d). Maximum $\delta^{13}C_z$ values for MIS 5e and 5d also occupy the same depth range (Figure 6). Benthic $\delta^{18}O$ values during MIS 5d are on average ~1‰ higher than MIS 5e (Figure 5c), but this is expected due to ice sheet expansion and high latitude cooling of 3–4°C (Kohfeld & Chase, 2017). Similar to the $\delta^{13}C$ results, the depth range of maximum $\delta^{18}O_z$ values overlap for MIS 5e and 5d (Figure 6). Overall, the Brazil Margin data indicate the depth of the NSW-SSW boundary remained stable during the MIS 5e-d transition. The lack of watermass shoaling in the $\delta^{18}O$ and $\delta^{13}C$ profiles during MIS 5d implies atmospheric CO_2 is not uniquely linked to Atlantic watermass geometry. Instead, surface ocean cooling, greater sea ice extent, and meltwater induced surface stratification may have lowered atmospheric CO_2 through reduced air-sea gas exchange (Kohfeld & Chase, 2017; Moore et al., 2000; Rutgers van der Loeff et al., 2014; Stephens & Keeling, 2000). An expanded area of negative surface buoyancy forcing in the Southern Ocean would presumably cause boundary shoaling, however (Ferrari et al., 2014). The absence of shoaling suggests sea ice extent and SSW volume are not necessarily coupled on glacial-interglacial timescales, consistent with our findings for MIS 5e. One other possibility is that surface cooling yielded higher preformed $\delta^{13}C$ for NSW and SSW through temperature dependent air-sea gas exchange (Broecker & Maier-Reimer, 1992; Lynch-Stieglitz et al., 1995). Such an effect could conceivably mask the effect of remineralization, yielding similar deep Atlantic $\delta^{13}C$ values for MIS 5e and 5d.

The change in watermass structure across the MIS 5a/4 transition is markedly different than MIS 5e/d. Similar to the other substages, the MIS 5a carbon isotope profile is characterized by a broad middepth $\delta^{13}C$ maximum between two $\delta^{13}C$ minima, that is, the classic pattern associated with interglacial intervals at the Brazil Margin (Figure 5d). The $\delta^{13}C$-inferred boundary between NSW and SSW is located between 2,700 m and 3,300 m during MIS 5a (Figure 6). The $\delta^{18}O$-inferred boundary for MIS 5a is shallower, between 2,000 and 2,500 m. One reason $\delta^{18}O$ and $\delta^{13}C$ could become decoupled is a lower endmember $\delta^{18}O$ value for SSW, which would reduce the $\delta^{18}O$ contrast with NSW and move the $\delta^{18}O$-inferred boundary upward in the water column. Alternatively, accumulation of remineralized carbon in the abyssal Atlantic would enhance the vertical $\delta^{13}C$ gradient, moving the $\delta^{13}C$-inferred boundary deeper. Regardless of the reason, the data indicate the NSW-SSW boundary was located below 2,000 m water depth during MIS 5a. By comparison, it was at or above 2,000 m during MIS 4 (Figure 6). Our results are consistent with published $\delta^{13}C$ and $[CO_3^{2-}]$ data that indicate much of the deep Atlantic was filled with ^{13}C-depleted watermass during MIS 4 (Kohfeld & Chase, 2017; Yu et al., 2016). The DIC signal required to explain the observed $[CO_3^{2-}]$ anomalies suggests that sequestration of carbon in the deep Atlantic can account for most of the drop in atmospheric CO_2 across the MIS 5a/4 transition (Yu et al., 2016). Thus, results for the MIS 5a/4 transition are consistent with shoaling of the watermass boundary, reduced mixing between SSW and NSW, and enhanced carbon sequestration in the abyss.

4.5. Driver of Lower $\delta^{13}C$ During the Last Interglacial Period

One of the main findings of this paper is that $\delta^{13}C$ during MIS 5e was more depleted throughout the water column than MIS 1. The MIS 5e−1 difference averages −0.8‰ above 2,000 m water depth and −0.3‰ below 2,000 m (Figure 5b). Lower $\delta^{13}C$ values in the 2,000–3,000 m range at the Brazil Margin may be due to AMOC weakening and reduced NSW influence at the Brazil Margin. The endmember $\delta^{13}C$ for NSW was also ∼0.3‰ lower during MIS 5e (Figure 11). Less NSW influence or a change in endmember composition should yield the largest anomalies in the depth range of NSW, however, which is inconsistent with the spatial pattern we observe in the $\delta^{13}C$ profile.

Records from the northeast Atlantic, equatorial Atlantic, southeast Atlantic, and eastern equatorial Pacific indicate oceanic $\delta^{13}C$ was ∼0.2‰ lower during MIS 5e than MIS 1 (Bengtson et al., 2021). Data compilations for the eastern Atlantic (Bouttes et al., 2020) and western Atlantic (Figure 9) also suggest $\delta^{13}C$ was systematically lighter during MIS 5e. The contrast in mean ocean $\delta^{13}C$ between MIS 5e and MIS 1 may be due to a long-term imbalance between weathering and deposition of calcium carbonate or organic carbon. Benthic foraminiferal $\delta^{13}C$ records from the deep Atlantic and Pacific display long-term trends during the late Pleistocene, with $\delta^{13}C$ increasing from ∼900 ka to 500 ka, decreasing from ∼500 ka to 250 ka, and increasing again from ∼250 ka to present (Elderfield et al., 2012; Lisiecki, 2014; Raymo et al., 1990; Wang et al., 2010). The overall signal (∼0.3‰) is comparable to the observed increase in mean $\delta^{13}C$ between MIS 6 and 2 (Oliver et al., 2010) and MIS 5e and 1 (this paper, Bengtson et al., 2021). As detailed in Jeltsch-Thömmes and Joos (2023), a simulated reduction in carbonate weathering results in a cascade of biogeochemical effects, starting with lower oceanic alkalinity and higher surface ocean pCO_2. This in turn enhances isotopic fractionation during photosynthesis, resulting in lower $\delta^{13}C$ of particulate organic carbon and therefore higher $\delta^{13}C$ of DIC ($\delta^{13}C_{DIC}$). A long-term (>100 kyr) trend in $\delta^{13}C_{DIC}$ of +0.3‰ can be achieved by reducing carbonate weathering by 40%. A similar $\delta^{13}C_{DIC}$ trend can be achieved by increasing organic carbon input to the ocean by 40%. Greater organic carbon flux initially causes lower $\delta^{13}C_{DIC}$ but it also yields higher surface ocean pCO_2. Similar to the carbonate weathering scenario, this enhances isotopic fractionation during marine photosynthesis, resulting in a long-term increase in $\delta^{13}C_{DIC}$ of ∼0.2‰ (Jeltsch-Thömmes & Joos, 2023). While the resulting signal is comparable to the observed $\delta^{13}C$ trend over the past 250 kyr, the required shifts in carbonate weathering and organic carbon fluxes are quite large. It is also unclear how changes in weathering or burial fluxes would create the depth-dependent $\delta^{13}C$ signal we observe at the Brazil Margin. Given persistent diapycnal mixing and oceanic overturning, it would appear that input of light carbon into the upper ocean is necessary to maintain the vertical gradient in $\delta^{13}C$ anomalies during MIS 5e, a time interval that lasted nearly 10 kyr. Burial fluxes of organic carbon and calcium carbonate could then remove the $\delta^{13}C$ anomaly over ∼100 kyr.

The depth-dependent $\delta^{13}C$ signal at the Brazil Margin may have been due to the input of isotopically light carbon into the upper ocean during MIS 5e. Model simulations suggest a 500 Pg injection of terrestrial carbon causes the mean ocean $\delta^{13}C$ to shift −0.2‰ within ∼1,000 years (Jeltsch-Thömmes & Joos, 2020). The $\delta^{13}C$ anomaly persists for approximately 10 ka before being slowly removed by the flux of organic matter and calcium carbonate to the seafloor, with the ocean returning to its original carbon isotopic composition in ∼100 kyr, similar to the elapsed time between MIS 5e and 1. The magnitude of the terrestrial carbon release is very large, however, equating to one-quarter of the modern terrestrial carbon reservoir (Holmén, 1992). Alternatively, the source of the pulse may have been volcanic CO_2 or methane. If volcanism were involved, the total carbon release would need to be roughly 3.5x larger (or ∼1,700 Pg) to account for the $\delta^{13}C$ difference between volcanic and terrestrial carbon (−7‰ vs. −24‰). While 2,000 Pg is trivial compared to the size of the mantle carbon reservoir (∼1×10^8 Pg; Dasgupta & Hirschmann, 2010), the only evidence for anomalous submarine volcanic activity during Termination II is a pronounced basaltic ash layer at the Pacific-Antarctic Ridge (Lund et al., 2018). Methane hydrates are also a possibility given that they are strongly depleted in ^{13}C (−40‰ to −90‰; Kvenvolden, 1993). Intermediate-depth $\delta^{13}C$ anomalies in the tropical Atlantic during TII and early MIS 5e have been attributed to AMOC-triggered subsurface warming and destabilization of methane clathrates (Weldeab et al., 2022). The ^{13}C-depleted signal could have been transmitted to the Brazil Margin along isopycnals, yielding the largest $\delta^{13}C$ anomalies at intermediate depths, similar to the observed pattern. The volcanic and clathrate sources remain hypothetical, however, with each requiring further documentation from a range of locations to assess their viability.

5. Conclusions

Vertical profiles of benthic $\delta^{18}O$ and $\delta^{13}C$ imply the volume of southern source water (SSW) in the Atlantic basin expanded during the LGM (Curry & Oppo, 2005; Keigwin, 2004). Shoaling of the boundary between SSW and northern source water (NSW) away from the zone of intense mixing near the sea floor should reduce mixing between the two watermasses, further isolating SSW and enhancing its ability to store carbon (Adkins, 2013; Lund et al., 2011). Expansion of SSW may be due to greater sea ice extent and negative buoyancy forcing in the Southern Ocean (Ferrari et al., 2014). If sea ice extent and SSW volume play a primary role in setting atmospheric CO_2 levels, then the boundary between NSW and SSW should follow a predictable pattern, with shoaling during glacial maxima and deepening during full interglacial conditions. We should also expect watermass boundary shoaling to occur during the two primary drops in atmospheric CO_2 of the last glacial cycle, the MIS 5a/4 and MIS 5e/d transitions. To test these predictions, we developed vertical profiles of $\delta^{18}O$ and $\delta^{13}C$ from the Brazil Margin to reconstruct the depth of the NSW-SSW boundary over the last glacial cycle. We also assess whether mixing between three primary watermasses (shallow SSW (sSSW), NSW, and SSW) can explain the Brazil Margin results.

Consistent with the anticipated glacial pattern, we find evidence for expansion of SSW during MIS 2, 4, and 6. Vertical profiles during glacial maxima MIS 2 and 6 are very similar to one another; the NSW-SSW watermass boundary was located near 2,500 m and there was an overall steepening of the vertical $\delta^{13}C$ gradient. During MIS 4 the NSW-SSW boundary was located shallower in the water column, near 2,000 m. Below this depth, persistently high $\delta^{18}O$ and low $\delta^{13}C$ document the expanded presence of SSW, consistent with published $\delta^{13}C$ compilations (Kohfeld & Chase, 2017; Oliver et al., 2010). Combined with carbonate ion reconstructions (Yu et al., 2016), the stable isotope data imply the drop in atmospheric CO_2 at MIS 5a/4 was likely due to expansion of SSW and accumulation of respired carbon at depth. Across MIS 5e/d, we see no evidence for expansion of SSW in the Brazil Margin $\delta^{18}O$ or $\delta^{13}C$ profiles, implying there was little change in Atlantic watermass geometry across this key transition. Thus, another factor must have been responsible for the drop in atmospheric CO_2 at the MIS 5e/d boundary, perhaps expanded sea ice cover in the Southern Ocean (Kohfeld & Chase, 2017). If such an expansion occurred, the associated change in surface buoyancy forcing apparently did not affect the volume of SSW in the deep South Atlantic.

Given the similarity in Brazil Margin watermass structure during MIS 2 and 6, one might also expect MIS 1 and 5e to be similar to one another. Yet the $\delta^{18}O$ and $\delta^{13}C$ profiles indicate the NSW-SSW boundary was at least 500 m shallower during MIS 5e than MIS 1, despite reduced sea ice extent in the Southern Ocean during the last interglacial period (Crosta et al., 2022; Holloway et al., 2017). Our results therefore do not support the hypothesis that all interglacial intervals are characterized by deepening of the watermass boundary and enhanced mixing between deep overturning cells. Additionally, we find that MIS 5e $\delta^{13}C$ values are systematically lighter throughout the water column than MIS 1, with the largest differences (~0.8‰) occurring above 2,000 m water depth. The Brazil Margin results are consistent with a positive shift in the mean $\delta^{13}C$ of the global ocean over the past ~250 kyr, as implied by $\delta^{13}C$ compilations from the Atlantic and Pacific basins (Bengtson et al., 2021; Lisiecki, 2014). The driver of the shift remains unclear, but the most plausible explanation is a long-term change in the weathering and burial of calcium carbonate or organic carbon (Jeltsch-Thömmes & Joos, 2020, 2023). Alternatively, the $\delta^{13}C$ signal may be due to input of carbon from a ^{13}C-depleted reservoir and its subsequent removal by the flux of organic matter and calcium carbonate to the seafloor.

Data Availability Statement

Supporting data from this manuscript can be found in the NOAA National Centers for Environmental Information Paleoclimate Database (Shub et al., 2023).

Acknowledgments
We would like to thank Patrick Rafter and one anonymous reviewer for comments on the manuscript. We would also like to thank Lora Wingate and Kacey Lohmann for their help with stable isotope analyses and Anna Mudahy and Sara McCart for their help with core sampling and foraminifera processing. We are grateful to the Woods Hole Oceanographic Institution core repository for curating the Brazil Margin cores. This work was supported by NSF Grant OCE-1804030.

References

Adkins, J. F. (2013). The role of deep ocean circulation in setting glacial climates. *Paleoceanography*, *28*(3), 539–561. https://doi.org/10.1002/palo.20046

Bengtson, S. A., Menviel, L. C., Meissner, K. J., Missiaen, L., Peterson, C. D., Lisiecki, L. E., & Joos, F. (2021). Lower oceanic $\delta^{13}C$ during the last interglacial period compared to the Holocene. *Climate of the Past*, *17*(1), 507–528. https://doi.org/10.5194/cp-17-507-2021

Böhm, E., Lippold, J., Gutjahr, M., Frank, M., Blaser, P., Antz, B., et al. (2015). Strong and deep Atlantic meridional overturning circulation during the last glacial cycle. *Nature*, *517*(7532), 73–76. https://doi.org/10.1038/nature14059

Bouttes, N., Vazquez Rivieros, N., Govin, A., Swingedouw, D., Sanchez-Goni, M. F., Crosta, X., & Roche, D. M. (2020). Carbon 13 isotopes reveal limited ocean circulation changes between interglacials of the last 800 ka. *Paleoceanography and Paleoclimatology*, *35*(5), e2019PA003776. https://doi.org/10.1029/2019PA003776

Broecker, W. S. (1982). Ocean chemistry during glacial time. *Geochimica et Cosmochimica Acta*, *46/10*(10), 1689–1705. https://doi.org/10.1016/0016-7037(82)90110-7

Broecker, W. S., & Maier-Reimer, E. (1992). The influence of air and sea exchange on the carbon isotope distribution in the sea. *Global Biogeochemical Cycles*, *6*(3), 315–320. https://doi.org/10.1029/92gb01672

Came, R. E., Oppo, D. W., & McManus, J. F. (2007). Amplitude and timing of temperature and salinity variability in the subpolar North Atlantic over the past 10 k.y. *Geology*, *35*(4), 315–318. https://doi.org/10.1130/G23455A.1

Capron, E., Govin, A., Feng, R., Otto-Bliesner, B. L., & Wolff, E. W. (2017). Critical evaluation of climate syntheses to benchmark CMIP6/PMIP4 127 ka Last Interglacial simulations in the high-latitude regions. *Quaternary Science Reviews*, *168*, 137–150. https://doi.org/10.1016/j.quascirev.2017.04.019

Capron, E., Govin, A., Stone, E. J., Masson-Delmotte, V., Mulitza, S., Otto-Bliesner, B., et al. (2014). Temporal and spatial structure of multi-millennial temperature changes at high latitudes during the Last Interglacial. *Quaternary Science Reviews*, *103*, 116–133. https://doi.org/10.1016/j.quascirev.2014.08.018

Channell, J. E. T., Hodell, D. A., & Lehman, B. (1997). Relative geomagnetic paleointensity and $\delta^{18}O$ at ODP Site 983 (Gardar Drift, North Atlantic) since 350 ka. *Earth and Planetary Science Letters*, *153*(1–2), 103–118. https://doi.org/10.1016/s0012-821x(97)00164-7

Clark, P. U., He, F., Golledge, N. R., Mitrovica, J. X., Dutton, A., Hoffman, J. S., & Dendy, S. (2020). Oceanic forcing of penultimate deglacial and last interglacial sea-level rise. *Nature*, *577*(7792), 660–664. https://doi.org/10.1038/s41586-020-1931-7

Crosta, X., Kohfeld, K. E., Bostock, H. C., Chadwick, M., Du Vivier, A., Esper, O., et al. (2022). Antarctic sea ice over the past 130,000 years - Part 1: A review of what proxy records tell us. *Climate of the Past*, *18*(8), 1729–1756. https://doi.org/10.5194/cp-18-1729-2022

Curry, W. B., & Oppo, D. W. (2005). Glacial water mass geometry and the distribution of $\delta^{13}C$ of ΣCO_2 in the western Atlantic Ocean. *Paleoceanography*, *20*(1), 1–12. https://doi.org/10.1029/2004PA001021

Dasgupta, R., & Hirschmann, M. M. (2010). The deep carbon cycle and melting in Earth's interior. *Earth and Planetary Science Letters*, *298*(1–2), 1–13. https://doi.org/10.1016/j.epsl.2010.06.039

Deaney, E. L., Barker, S., & van de Flierdt, T. (2017). Timing and nature of AMOC recovery across Termination 2 and magnitude of deglacial CO_2 change. *Nature Communications*, *8*(1), 14595. https://doi.org/10.1038/ncomms14595

Du, J., Haley, B. A., & Mix, A. C. (2020). Evolution of the Global Overturning Circulation since the Last Glacial Maximum based on marine authigenic neodymium isotopes. *Quaternary Science Reviews*, *241*, 106396. https://doi.org/10.1016/j.quascirev.2020.106396

Duplessy, J., Shackleton, N. J., Matthews, R. K., Prell, W., Ruddiman, W. F., Caralp, M., & Hendy, C. H. (1984). ^{13}C Record of benthic foraminifera in the last interglacial ocean: Implications for the carbon cycle and the global deep water circulation. *Quaternary Research*, *21*(2), 225–243. https://doi.org/10.1016/0033-5894(84)90099-1

Dyer, B., Austermann, J., D'Andrea, W. J., Creel, R. C., Sandstrom, M. R., Cashman, M., et al. (2021). Sea-level trends across The Bahamas constrain peak last interglacial ice melt. *Proceedings of the National Academy of Sciences*, *118*(33), e2026839118. https://doi.org/10.1073/pnas.2026839118

Eggleston, S., Schmitt, J., Bereiter, B., Schneider, R., & Fischer, H. (2016). Evolution of the stable carbon isotope composition of atmospheric CO_2 over the last glacial cycle. *Paleoceanography*, *31*(3), 434–452. https://doi.org/10.1002/2015PA002874

Elderfield, H., Ferretti, P., Greaves, M., Crowhurst, S., McCave, I. N., Hodell, D., & Piotrowski, A. M. (2012). Evolution of ocean temperature and ice volume through the mid-Pleistocene climate transition. *Science*, *337*(6095), 704–709. https://doi.org/10.1126/science.1221294

Ferrari, R., Jansen, M. F., Adkins, J. F., Burke, A., Stewart, A. L., & Thompson, A. F. (2014). Antarctic sea ice control on ocean circulation in present and glacial climates. *Proceedings of the National Academy of Sciences*, *111*(24), 8753–8758. https://doi.org/10.1073/pnas.1323922111

Garity, M., Lund, D., & Shub, A. (2024). Multi-proxy evidence for Atlantic Meridional Overturning Circulation (AMOC) weakening during deglaciations of the past 150,000 years. *Paleoceanography and Paleoclimatology*. https://doi.org/10.1029/2023PA004629

Gebbie, G. (2014). How much did Glacial North Atlantic Water shoal? *Paleoceanography*, *29*(3), 190–209. https://doi.org/10.1002/2013PA002557

Genthon, G., Barnola, J., Raynaud, D., Lorius, C., Jouzel, J., Barkov, N. I., et al. (1987). Vostok ice core: Climatic response to CO_2 and orbital forcing changes over the last climatic cycle. *Nature*, *329*(6138), 414–418. https://doi.org/10.1038/329414a0

Gottschalk, J., Vázquez Riveiros, N., Waelbroeck, C., Skinner, L. C., Michel, E., Duplessy, J., et al. (2016). Carbon isotope offsets between benthic foraminifer species of the genus Cibicides (Cibicidoides) in the glacial sub-Antarctic Atlantic. *Paleoceanography*, *31*(12), 1583–1602. https://doi.org/10.1002/2016PA003029

Haslett, J., & Parnell, A. (2008). A simple monotone process with application to radiocarbon-dated depth chronologies. *Journal of the Royal Statistical Society: Series C (Applied Statistics)*, *57*(4), 399–418. https://doi.org/10.1111/j.1467-9876.2008.00623.x

Heaton, T. J., Köhler, P., Butzin, M., Bard, E., Reimer, R. W., Austin, W. E. N., et al. (2020). Marine20—The marine radiocarbon age calibration curve (0–55,000 cal BP). *Radiocarbon*, *62*(4), 779–820. https://doi.org/10.1017/RDC.2020.68

Hodell, D. A., Charles, C. D., Curtis, J. H., Mortyn, P., Ninnemann, U., & Venz, K. A. (2003). Data report: Oxygen isotope stratigraphy of ODP Leg 177 Sites 1088, 1089, 1090, 1093, and 1094. *Proceedings of the Ocean Drilling Program Scientific Results*, *177*, 1–26. https://doi.org/10.2973/odp.proc.sr.177.120.2003

Hoffman, J. L., & Lund, D. C. (2012). Refining the stable isotope budget for Antarctic Bottom Water: New foraminiferal data from the abyssal southwest Atlantic. *Paleoceanography*, *27*(1), PA1213. https://doi.org/10.1029/2011PA002216

Hoffman, J. S., Clark, P. U., Parnell, A. C., & He, F. (2017). Regional and global sea-surface temperatures during the last interglaciation. *Science*, *355*(6322), 276–279. https://doi.org/10.1126/science.aai8464

Holloway, M. D., Sime, L. C., Allen, C. S., Hillenbrand, C., Bunch, P., Wolff, E., & Valdes, P. J. (2017). The spatial structure of the 128 ka Antarctic sea ice minimum. *Geophysical Research Letters*, *44*(21), 11129–11139. https://doi.org/10.1002/2017GL074594

Holloway, M. D., Sime, L. C., Singarayer, J. S., Tindall, J. C., & Valdes, P. J. (2018). Simulating the 128-ka Antarctic Climate Response to Northern Hemisphere Ice Sheet Melting Using the Isotope-Enabled HadCM3. *Geophysical Research Letters*, *45*(21), 11921–11929. https://doi.org/10.1029/2018GL079647

Holmén, K. (1992). The global carbon cycle. *International Geophysics*, *50*, 239–262. https://doi.org/10.1016/S0074-6142(08)62694-7

Huybers, P., & Wunsch, C. (2005). Obliquity pacing of the late Pleistocene glacial terminations. *Nature*, *434*(7032), 491–494. https://doi.org/10.1038/nature03401

Imbrie, J., Boyle, E. A., Clemens, S. C., Duffy, A., Howard, W. R., Kukla, G., et al. (1992). On the structure and origin of major glaciation cycles 1. Linear responses to Milankovitch forcing. *Paleoceanography*, *7*(6), 701–738. https://doi.org/10.1029/92PA02253

Indermühle, A., Stauffer, B., Stocker, T. F., Raynaud, D., & Barnola, J. (1999). Early Holocene atmospheric CO_2 concentrations. *Science*, *286*(5446), 1815. https://doi.org/10.1126/science.286.5446.1815a

Jaccard, S. L., Galbraith, E. D., Martínez-García, A., & Anderson, R. F. (2016). Covariation of deep Southern Ocean oxygenation and atmospheric CO_2 through the last ice age. *Nature*, *530*(7589), 207–210. https://doi.org/10.1038/nature16514

Jackett, D. R., & McDougall, T. J. (1997). A neutral density variable for the world's oceans. *Journal of Physical Oceanography*, *27*(2), 237–263. https://doi.org/10.1175/1520-0485(1997)027<0237:andvft>2.0.co;2

Jeltsch-Thömmes, A., & Joos, F. (2020). Modeling the evolution of pulse-like perturbations in atmospheric carbon and carbon isotopes: The role of weathering-sedimentation imbalances. *Climate of the Past*, *16*(2), 423–451. https://doi.org/10.5194/cp-16-423-2020

Jeltsch-Thömmes, A., & Joos, F. (2023). Carbon cycle responses to changes in weathering and the long-term fate of stable carbon isotopes. *Paleoceanography and Paleoclimatology*, *38*(2), e2022PA004577. https://doi.org/10.1029/2022PA004577

Keigwin, L. D. (2004). Radiocarbon and stable isotope constraints on Last Glacial Maximum and Younger Dryas ventilation in the western North Atlantic. *Paleoceanography*, *19*(4), PA4012. https://doi.org/10.1029/2004PA001029

Khatiwala, S., Schmittner, A., & Muglia, J. (2019). Air-sea disequilibrium enhances ocean carbon storage during glacial periods. *Science Advances*, *5*(6), eaaw4981. https://doi.org/10.1126/sciadv.aaw4981

Kohfeld, K. E., & Chase, Z. (2017). Temporal evolution of mechanisms controlling ocean carbon uptake during the last glacial cycle. *Earth and Planetary Science Letters*, *472*, 206–215. https://doi.org/10.1016/j.epsl.2017.05.015

Kvenvolden, K. A. (1993). Gas hydrates—Geological perspective and global change. *Reviews of Geophysics*, *31*(2), 173–187. https://doi.org/10.1029/93RG00268

Lisiecki, L. E. (2014). Atlantic overturning responses to obliquity and precession over the last 3 Myr. *Paleoceanography*, *29*(2), 71–86. https://doi.org/10.1002/2013PA002505

Lisiecki, L. E., & Stern, J. V. (2016). Regional and global benthic $\delta^{18}O$ stacks for the last glacial cycle. *Paleoceanography*, *31*(10), 1368–1394. https://doi.org/10.1002/2016PA003002

Lumpkin, R., & Speer, K. (2007). Global ocean meridional overturning. *Journal of Physical Oceanography*, *37*(10), 2550–2562. https://doi.org/10.1175/JPO3130.1

Lund, D. C., Adkins, J. F., & Ferrari, R. (2011). Abyssal Atlantic circulation during the Last Glacial Maximum: Constraining the ratio between transport and vertical mixing. *Paleoceanography*, *26*(1), PA1213. https://doi.org/10.1029/2010PA001938

Lund, D. C., Seeley, E. I., Asimow, P. D., Lewis, M. J., McCart, S. E., & Mudahy, A. A. (2018). Anomalous Pacific-Antarctic Ridge Volcanism Precedes Glacial Termination 2. *Geochemistry, Geophysics, Geosystems*, *19*(8), 2478–2491. https://doi.org/10.1029/2017GC007341

Lund, D. C., Tessin, A. C., Hoffman, J. L., & Schmittner, A. (2015). Southwest Atlantic water mass evolution during the last deglaciation. *Paleoceanography*, *30*(5), 477–494. https://doi.org/10.1002/2014PA002657

Lüthi, D., Le Floch, M., Bereiter, B., Blunier, T., Barnola, J., Siegenthaler, U., et al. (2008). High-resolution carbon dioxide concentration record 650,000–800,000 years before present. *Nature*, *453*(7193), 379–382. https://doi.org/10.1038/nature06949

Lynch-Stieglitz, J., Stocker, T. F., Broecker, W. S., & Fairbanks, R. G. (1995). The influence of air-sea exchange on the isotopic composition of oceanic carbon: Observations and modeling. *Global Biogeochemical Cycles*, *9*(4), 653–665. https://doi.org/10.1029/95GB02574

Marchal, O., & Curry, W. B. (2008). On the abyssal circulation in the glacial Atlantic. *Journal of Physical Oceanography*, *38*(9), 2014–2037. https://doi.org/10.1175/2008JPO3895.1

Marchitto, T. M., Curry, W. B., Lynch-Stieglitz, J., Bryan, S. P., Cobb, K. M., & Lund, D. C. (2014). Improved oxygen isotope temperature calibrations for cosmopolitan benthic foraminifera. *Geochimica et Cosmochimica Acta*, *130*, 1–11. https://doi.org/10.1016/j.gca.2013.12.034

Marshall, J., & Speer, K. (2012). Closure of the meridional overturning circulation through Southern Ocean upwelling. *Nature Geoscience*, *5*(3), 171–180. https://doi.org/10.1038/ngeo1391

Martínez-García, A., Sigman, D. M., Ren, H., Anderson, R. F., Straub, M., Hodell, D. A., et al. (2014). Iron fertilization of the Subantarctic Ocean during the last ice age. *Science*, *343*(6177), 1347–1350. https://doi.org/10.1126/science.1246848

Moore, J. K., Abbott, M. R., Richman, J. G., & Nelson, D. M. (2000). The Southern Ocean at the Last Glacial Maximum: A strong sink for atmospheric carbon dioxide. *Global Biogeochemical Cycles*, *14*(1), 455–475. https://doi.org/10.1029/1999GB900051

Morales Maqueda, M. A., & Rahmstorf, S. (2002). Did Antarctic sea-ice expansion cause glacial CO_2 decline? *Geophysical Research Letters*, *29*(1), 11–13. https://doi.org/10.1029/2001GL013240

Neftel, A., Oeschger, H., Schwander, J., Stauffer, B., & Zumbrunn, R. (1982). Ice core sample measurements give atmospheric CO_2 content during the past 40,000 yr. *Nature*, *295*(5846), 220–223. https://doi.org/10.1038/295220a0

Oliver, K. I. C., Hoogakker, B. A. A., Crowhurst, S., Henderson, G. M., Rickaby, R. E. M., Edwards, N. R., & Elderfield, H. (2010). A synthesis of marine sediment core $\delta^{13}C$ data over the last 150,000 years. *Climate of the Past*, *6*(5), 645–673. https://doi.org/10.5194/cp-6-645-2010

Oppo, D. W., Gebbie, G., Huang, K., Curry, W. B., Marchitto, T. M., & Pietro, K. R. (2018). Data constraints on glacial Atlantic water mass geometry and properties. *Paleoceanography and Paleoclimatology*, *33*(9), 1013–1034. https://doi.org/10.1029/2018PA003408

Oppo, D. W., Horowitz, M., & Lehman, S. J. (1997). Marine core evidence for reduced deep water production during Termination II followed by a relatively stable substage 5e (Eemian). *Paleoceanography*, *12*(1), 51–63. https://doi.org/10.1029/96PA03133

Oppo, D. W., Keigwin, L. D., McManus, J. F., & Cullen, J. L. (2001). Persistent suborbital climate variability in marine isotope stage 5 and termination II. *Paleoceanography*, *16*(3), 280–292. https://doi.org/10.1029/2000PA000527

Ostermann, D. R., & Curry, W. B. (2000). Calibration of stable isotopic data: An enriched $\delta^{18}O$ standard used for source gas mixing detection and correction. *Paleoceanography*, *15*(3), 353–360. https://doi.org/10.1029/1999PA000411

Otto-Bliesner, B., Rosenbloom, N., Stone, E. J., McKay, N. P., Lunt, D. J., Brady, E. C., & Overpeck, J. T. (2013). How warm was the last interglacial? New model–data comparisons. *Philosophical Transactions of the Royal Society A: Mathematical, Physical & Engineering Sciences*, *371*(2001), 20130097. https://doi.org/10.1098/rsta.2013.0097

Petit, J. R., Jouzel, J., Raynaud, D., Barkov, N. I., Barnola, J., Basile, I., et al. (1999). Climate and atmospheric history of the past 420,000 years from the Vostok ice core, Antarctica. *Nature*, *399*(6735), 429–436. https://doi.org/10.1038/20859

Polzin, K. L., Toole, J. M., Ledwell, J. R., & Schmitt, R. W. (1997). Spatial variability of Turbulent mixing in the abyssal ocean. *Science*, *276*(5309), 93–96. https://doi.org/10.1126/science.276.5309.93

Pöppelmeier, F., Blaser, P., Gutjahr, M., Jaccard, S. L., Frank, M., Max, L., & Lippold, J. (2020). Northern-sourced water dominated the Atlantic Ocean during the Last Glacial Maximum. *Geology*, *48*(8), 826–829. https://doi.org/10.1130/G47628.1

Praetorius, S. K., McManus, J. F., Oppo, D. W., & Curry, W. B. (2008). Episodic reductions in bottom-water currents since the last ice age. *Nature Geoscience*, *1*(7), 449–452. https://doi.org/10.1038/ngeo227

Railsback, L. B., Gibbard, P. L., Head, M. J., Voarintsoa, N. R. G., & Toucanne, S. (2015). An optimized scheme of lettered marine isotope substages for the last 1.0 million years, and the climatostratigraphic nature of isotope stages and substages. *Quaternary Science Reviews*, *111*, 94–106. https://doi.org/10.1016/j.quascirev.2015.01.012

Raymo, M. E., Oppo, D. W., Flower, B. P., Hodell, D. A., McManus, J. F., Venz, K. A., et al. (2004). Stability of North Atlantic water masses in face of pronounced climate variability during the Pleistocene. *Paleoceanography*, *19*(2), 1–13. https://doi.org/10.1029/2003PA000921

Raymo, M. E., Ruddiman, W. F., Shackleton, N. J., & Oppo, D. W. (1990). Evolution of the Atlantic-Pacific $\delta^{13}C$ gradients over the last 2.5 m.y. *Earth and Planetary Science Letters*, *97*(3–4), 353–368. https://doi.org/10.1016/0012-821x(90)90051-x

Reimer, P. J., Austin, W. E. N., Bard, E., Bayliss, A., Blackwell, P. G., Bronk Ramsey, C., et al. (2020). The IntCal20 Northern Hemisphere radiocarbon age calibration curve (0–55 cal kBP). *Radiocarbon*, *62*(4), 725–757. https://doi.org/10.1017/RDC.2020.41

Reimer, P. J., & Reimer, R. W. (2001). A marine reservoir correction database and on-line interface. *Radiocarbon*, *43*(2A), 461–463. https://doi.org/10.1017/S0033822200038339

Rutgers van der Loeff, M., Cassar, N., Nicolaus, M., Rabe, B., & Stimac, I. (2014). The influence of sea ice cover on air-sea gas exchange estimated with radon-222 profiles. *Journal of Geophysical Research: Oceans*, *119*, 8410–8421. https://doi.org/10.1002/2013JC009321

Schlitzer, R. (2000). Electronic Atlas of WOCE hydrographic and tracer data now available. *Eos, Transactions American Geophysical Union*, *81*(5), 45. https://doi.org/10.1029/00eo00028

Schmittner, A., Bostock, H. C., Cartapanis, O., Curry, W. B., Filipsson, H. L., Galbraith, E. D., et al. (2017). Calibration of the carbon isotope composition ($\delta^{13}C$) of benthic foraminifera. *Paleoceanography*, *32*(6), 512–530. https://doi.org/10.1002/2016PA003072

Shakun, J. D., Clark, P. U., He, F., Marcott, S. A., Mix, A. C., Liu, Z., et al. (2012). Global warming preceded by increasing carbon dioxide concentrations during the last deglaciation. *Nature*, *484*(7392), 49–54. https://doi.org/10.1038/nature10915

Shub, A. B., Lund, D. C., Oppo, D. W., & Garity, M. L. (2023). NOAA/WDS Paleoclimatology - Brazil Margin Stable Isotope Data for the Last Glacial Cycle [Dataset]. NOAA National Centers for Environmental Information. https://doi.org/10.25921/n443-0561

Sigman, D. M., & Boyle, E. A. (2000). Glacial/interglacial variations in atmospheric carbon dioxide in Atmospheric Carbon Dioxide. *Nature*, *407*, 859–869. https://doi.org/10.1038/35038000

Sikes, E. L., Allen, K. A., & Lund, D. C. (2017). Enhanced $\delta^{13}C$ and $\delta^{18}O$ differences between the South Atlantic and South Pacific during the last glaciation: The deep Gateway hypothesis. *Paleoceanography*, *32*(10), 1000–1017. https://doi.org/10.1002/2017PA003118

Sortor, R. N., & Lund, D. C. (2011). No evidence for a deglacial intermediate water $\Delta^{14}C$ anomaly in the SW Atlantic. *Earth and Planetary Science Letters*, *310*(1), 65–72. https://doi.org/10.1016/j.epsl.2011.07.017

Stephens, B. B., & Keeling, R. F. (2000). The influence of Antarctic Sea ice on glacial-interglacial CO_2 variations. *Nature*, *404*(6774), 171–174. https://doi.org/10.1038/35004556

St. Laurent, L. C., Simmons, H. L., & Jayne, S. R. (2002). Estimating tidally driven mixing in the deep ocean. *Geophysical Research Letters*, *29*(23), 21-1–21-4. https://doi.org/10.1029/2002GL015633

Tessin, A. C., & Lund, D. C. (2013). Isotopically depleted carbon in the mid-depth South Atlantic during the last deglaciation. *Paleoceanography*, *28*(2), 296–306. https://doi.org/10.1002/palo.20026

Toggweiler, J. R. (1999). Variation of atmospheric CO_2 by ventilation of the ocean's deepest water. *Paleoceanography*, *14*(5), 571–588. https://doi.org/10.1029/1999PA900033

Turney, C. S. M., & Jones, R. T. (2010). Does the Agulhas Current amplify global temperatures during super-interglacials? *Journal of Quaternary Science*, *25*(6), 839–843. https://doi.org/10.1002/jqs.1423

Waelbroeck, C., Skinner, L. C., Labeyrie, L., Duplessy, J. C., Michel, E., Riveiros, N. V., et al. (2011). The timing of deglacial circulation changes in the Atlantic. *Paleoceanography*, *26*(3), 1–10. https://doi.org/10.1029/2010PA002007

Wang, P., Tian, J., & Lourens, L. J. (2010). Obscuring of long eccentricity cyclicity in Pleistocene oceanic carbon isotope records. *Earth and Planetary Science Letters*, *290*(3), 319–330. https://doi.org/10.1016/j.epsl.2009.12.028

Weldeab, S., Schneider, R. R., Yu, J., & Kylander-Clark, A. (2022). Evidence for massive methane hydrate destabilization during the penultimate interglacial warming. *Proceedings of the National Academy of Sciences*, *119*(35), e2201871119. https://doi.org/10.1073/pnas.2201871119

Wunsch, C., & Ferrari, R. (2004). Vertical mixing, energy, and the general circulation of the oceans. *Annual Review of Fluid Mechanics*, *36*(1), 281–314. https://doi.org/10.1146/annurev.fluid.36.050802.122121

Yin, Q. Z., & Berger, A. (2011). Individual contribution of insolation and CO_2 to the interglacial climates of the past 800,000 years. *Climate Dynamics*, *38*(3–4), 709–724. https://doi.org/10.1007/s00382-011-1013-5

Yu, J., Menviel, L., Jin, Z. D., Thornalley, D. J. R., Barker, S., Marino, G., et al. (2016). Sequestration of carbon in the deep Atlantic during the last glaciation. *Nature Geoscience*, *9*(4), 319–324. https://doi.org/10.1038/ngeo2657